Nonadiabatic molecular dynamics simulation of ultrafast pump-probe experiments on I$_2$ in solid rare gases

V. S. Batista[a)]
Department of Chemistry, Boston University, 590 Commonwealth Avenue, Boston, Massachusetts 02215

D. F. Coker
Department of Chemistry, Boston University, 590 Commonwealth Avenue, Boston, Massachusetts 02215
and Centre Européen de Calcul Atomique et Moléculair, CECAM, ENS Lyon, 46 Allée d'Italie,
69364 Lyon Cedex 07, France

Recent experimental studies of both *A* and *B* state photoexcitation of I$_2$ and the ensuing many-body dynamics in rare gas matrices by Apkarian and co-workers are simulated using the methods we presented in an earlier work combining nonadiabatic molecular dynamics with semiempirical diatomics-in-molecules (DIM) excited state electronic structure techniques. We extend our DIM methods to compute the ion pair states of the I$_2$-rare gas crystal system and use these states together with a model of the configurational dependence of the electronic dipole operator matrix elements to calculate the time resolved probe absorption signals in these pump - probe experiments using a simple golden rule result. Our computed signals are in remarkable agreement with experiments and we use our calculations to provide a detailed microscopic analysis of the channels to predissociation and recombination underlying these experiments. © *1997 American Institute of Physics.* [S0021-9606(97)02017-5]

I. INTRODUCTION

Ultrafast spectroscopic studies of molecular photodissociation over a range of solvent conditions from gases to the condensed phases enable detailed interrogation of the dynamics of breaking and remaking of chemical bonds, and the influence of solvent environment on these fundamental chemical processes. A very large body of work including both time independent, and time resolved spectroscopic experiments, as well as analytic theories and molecular dynamics simulations[1–7] [see Ref. (1) for other references to this theoretical and computational work], has been devoted to the study of diatomic molecular photodissociation, in particular the photodissociation of I$_2$, in clusters,[8–13] solids,[14–16] liquids,[1,17–24] and high pressure gases[25–29] composed of nonpolar molecules ranging from simple rare gas atoms to more complex polyatomic solvents such as cyclohexane and benzene.[30]

The interpretation of much of this work is complicated by two related issues: First, despite the fact that many of the gas phase potential surfaces for I$_2$ are known quite accurately, the perturbation of these surfaces due to the presence of the solvent environment has only recently become ammenable to detailed study through the application of semiempirical electronic structure methods to these complex many-body interactions.[1,31–37] Secondly, these processes are fundamentally electronically nonadiabatic so the dynamics which governs dissociation of the molecule on a repulsive surface, and its subsequent recombination into a bound electronic state necessarily involves nonadiabatic motion over perhaps many coupled electronic surfaces. Computational methods for treating this type of nonadiabatic dynamics in an accurate and reliable way have only recently been developed.[38–41]

In a recent paper[1] we showed how semiempirical diatomics-in-molecules (DIM) electronic structure techniques could be combined with nonadiabatic molecular dynamics methods to provide an accurate general overview of I$_2$ *B* state predissociation and subsequent geminate recombination dynamics in liquid xenon consistent with experimental findings. We found that these methods provided a reasonable description of the influence of solvent on the nonadiabatic couplings between electronic states and showed that these techniques gave subpicosecond timescales for predissociation and recombination, as well as relaxation pathways which were in good agreement with experimental findings.

In this article we address the more ambitious task of computing specific experimental spectra using these methods and provide a first principles understanding of the effect of many-body interactions on nonadiabatic dynamics which is in general the underlying challenge of condensed phase reactive dynamics. We will focus on the simulation of time resolved pump-probe signals from I$_2$ in rare gas matrices following excitation of the I$_2$ to either its $A(^3\Pi_{1u})$ or $B[^3\Pi_u(0^+)]$ excited electronic states. After excitation by the pump pulse, the I atom fragments move apart due to the repulsive nature of these excited state surfaces in the Franck–Condon region. In the gas phase, the I atoms would separate to infinity, yielding a unit probability of photodissociation. In the solid, however, the lattice prevents permanent dissociation by caging the photofragments. Unlike the case in liquids and van der Waals clusters, cage-induced recombination of I$_2$ proceeds with unit probability in solid rare gas matrices.

[a)]Present address: Department of Chemistry, University of California, Berkeley, CA 94720.

The microscopic dynamics of these photodissociation and recombination processes can in principle be explored in detail using ultrafast time resolved pump-probe experiments,[11,17,24,42] in which a delayed probe pulse interrogates the evolving mixed excited state by promoting the system to even higher energy electronic excited states and watching when and where these probe excitations take place. For I_2 in rare gas matrices this probing can be viewed approximately as excitation from some transient mixture of states (including the A, A', X, B, or some predissociative intermediate state) to various possible solvated ion pair final excited states. The experimental observable in these studies is the laser induced fluorescence from these final ion-pair states as a function of pump-probe delay.

In a series of recent experiments,[15,42–45] Apkarian and co-workers reported time resolved pump-probe measurements on I_2 isolated in Ar and Kr cryogenic matrices and showed that vibrational populations created by ultrashort laser pulses retained their coherence for more than 5 ps after photoexcitation to the A or B states. These surprising findings of relaxation timescales in the solid which are more than an order of magnitude longer than typical timings for predissociation and geminate recombination of I_2 in liquids must be understood in terms of molecular vibrations created through the sequence of photodissociation, collision with the host cage, energy loss, recoil, and recombination.[45] Despite the rich information content in experimental pump-probe data, the signals are the result of complex many-body dynamics, the details of which cannot be extracted by a cursory examination of the results.[45] It is thus essential to combine the experimental studies with theoretical simulations that face the challenge of yielding a comprehensive understanding of the signals and their underlying dynamics.

Early molecular dynamics (MD) simulations were restricted to studies of vibrational relaxation[46–48] or adiabatic caging[5–7,42,44] where nonadiabatic dynamics was completely disregarded and pairwise additive interactions were assumed. In this article we will demonstrate that the molecular dynamics involved in these microscopic processes is fundamentally nonadiabatic, and that the interactions of the open shell species (the separating I atoms) with the surrounding condensed phase environment which are responsible for the nonadiabatic couplings are explicitly many-body in nature.[1,32,43]

The article is organized as follows: Our preparation of the nonadiabatic MD ensemble of initial conditions consistent with vertical pump excitation is first described in Sec. II A. Next, in Sec. II B our application of the golden rule to computing the pump-probe signals from our ensemble of nonadiabatic surface hopping trajectories is outlined. Section II C describes our calculation of the ion pair states using the diatomics-in-ionic-systems (DIIS) extension of the DIM method. For a description of our nonadiabatic MD methods and DIM calculations of the covalent state manifolds we refer the reader to Ref. 1. In Sec. II D we detail the model of the dipole operator matrix elements used in our calculations of the signals. Section III presents our results for initial excitation I_2 in solid argon to both its A state (Sec. III A), and its B state (Sec. III B) and makes detailed comparisons with

available experimental results. In Sec. III C we explore the effect of changing the matrix from argon to xenon predicted by our calculations and the article is finally concluded in Sec. IV.

II. METHODS

A. Sample preparation and photoexcitation

The approach we employ for computing the experimental pump-probe signals involves first generating equilibrium solvent configurations of the ground state I_2-rare gas matrix system for which the experimental pump frequencies are resonant with the energy difference between the ground X state and either the A or B excited states. Ensembles of 72 independent trajectories are first equilibrated for about 10 ps at $T = 40$ K in the argon matrix. Each individual trajectory is started from an undistorted fcc crystal of 108 argon atoms with an I_2 molecule in a double substitutional site.[42,49] Due to the fact that an I_2 molecule is considerably larger than an argon atom it fits perfectly in such a cavity which is created by removing two nearest neighbor argon atoms. Despite the fact that xenon atoms are much larger than argon atoms, the long axis of the I_2 molecule is still at least 40% larger than the xenon atom diameter. As such we have also initiated our studies of photoexcitation of I_2 in zero pressure xenon matrices ($\rho^* = 1.16$) reported in Sec. III from configurations along an equilibrated trajectory of an I_2 molecule in a double substitutional site in the xenon matrix.

Each of these ground state equilibrated trajectories is then evolved adiabatically in the X state until the pump resonance condition is achieved. These pump resonant configurations are used as independent initial conditions for vertical photoexcitation to the appropriate A or B states, leaving all coordinates and velocities unchanged. The electronic expansion coefficient vectors are set to the appropriate initial unit vectors for the relevant photoexcitation in each ensemble member and the nonadiabatic MD methods coupled with the DIM techniques presented in Ref. 1 are used to evolve the photoexcited ensemble of surface hopping trajectories consistent with the coherently propagated dynamical mixed state electronic wavefunction for each trajectory. Mixed state excitations are possible within our formulation but we have not considered them in these studies.

The 72 ensemble members for each calculation reported here were actually run in 4 groups of 18. The qualitative behavior of our calculated signals averaged over the full ensemble and reported in Sec. III is actually reproduced in each smaller group of trajectories, thus adding more ensemble members just smooths our results rather than introducing any qualitatively new types of dynamics. We thus believe that for this system our relatively small sample of trajectories gives statistically meaningful qualitative results.

B. Method for calculating pump-probe signals

Calculating the subsequent probe absorption signals necessarily involves the calculation of the upper ion pair states as well as the dipole operator matrix elements, μ_{if}, which

couple these ion pair states to the various covalent states occupied as a result of the excited state nonadiabatic dynamics. The calculation of these states and the dipole operator matrix elements are detailed in Secs. II C and II D. These results are then used in the following golden rule expression for the bare signal, $S(t)$, with time delay t between the pump and probe pulses:

$$S(t) \sim \sum_i \sum_f \int d\mathbf{R} \rho_i(\mathbf{R},t) |\mu_{if}^{ad}(\mathbf{R})|^2 \delta(\Delta V_{if}(\mathbf{R}) - h\nu_{probe}). \tag{2.1}$$

Here $\rho_i(\mathbf{R},t)$ is the nonequilibrium time dependent probability density that the absorption transition takes place from initial adiabatic state i at nuclear configuration $\mathbf{R}$, μ_{if}^{ad} are the $\mathbf{R}$-dependent electronic transition dipole operator matrix elements between the adiabatic states, and the energy conserving δ function counts only configurations for which the probe resonance condition, $\Delta V_{if}(\mathbf{R}) = V_f^{ion}(\mathbf{R}) - V_i^{cov}(\mathbf{R}) = h\nu_{probe}$, is satisfied. Here ν_{probe} is the probe frequency and $V_i^{cov}(\mathbf{R})$ and $V_f^{ion}(\mathbf{R})$ are the covalent and ion pair adiabatic state energies, respectively. Use of this golden rule expression to compute probe signals assumes that the nuclear framework remains stationary during the probe electronic excitation.

Our ensemble of N surface hopping trajectories is distributed among the adiabatic states according to the coherent evolution of the dynamical mixed state electronic wavefunction. With this representation the time dependent nonequilibrium probability density of occupying adiabatic state i at time t is simply

$$\rho_i(\mathbf{R},t) = \frac{1}{N}\sum_{k=1}^{N} \delta_{j_k i}\delta[\mathbf{R} - \mathbf{R}_k(t)], \tag{2.2}$$

where the sum is over the ensemble of N surface hopping trajectories, with trajectory k at position $\mathbf{R}_k(t)$ and occupying adiabatic electronic state j_k at time t.

Substituting into Eq. (2.1) and integrating over nuclear coordinates we obtain the signal as an average over our ensemble of surface hopping trajectories

$$S(t) \sim \frac{1}{N}\sum_{k=1}^{N} \sum_f |\mu_{fj_k}^{ad}[\mathbf{R}_k(t)]|^2 \delta\{\Delta V_{fj_k}[\mathbf{R}_k(t)] - h\nu_{probe}\}. \tag{2.3}$$

Due to the finite duration of the assumed Gaussian shaped probe pulse in time, its frequency spectrum is non-monochromatic. We model this frequency distribution as a transform limited Gaussian in probe pulse energy so accounting for the finite energy spread of the probe pulse and we write the signal as

$$S(t) \sim \frac{1}{N}\sum_{k=1}^{N} \sum_f |\mu_{fj_k}^{ad}[\mathbf{R}_k(t)]|^2$$
$$\times \exp[-\{\Delta V_{fj_k}[\mathbf{R}_k(t)] - h\nu_{probe}\}^2/2\sigma^2]. \tag{2.4}$$

Finally, to take account of the finite time duration of the pump pulse we convolve the bare signal $S(t)$ with the pump

pulse shape modeled as a Gaussian of 150 fs FWHM (i.e., $\delta = 63.7$ fs). Our final expression for the experimental signal is thus obtained as

$$\sigma(t) \approx \int_{-\infty}^{\infty} dt' \exp\frac{(t-t')^2}{2\delta^2} S(t'). \tag{2.5}$$

C. Diatomics-in-ionic-systems calculation of ion pair states

In this section we present our implementation of the diatomics-in-ionic systems method (DIIS) for computing potential energy surfaces (PES) of covalent and electron transfer ion pair molecular states of an I_2 molecule embedded in solid argon. This semiempirical approach is the diatomics-in-molecules (DIM) method[50–52] supplemented by classical expressions for the induction energy and has been successfully investigated by Last et al.[34] in studies of chlorine atoms embedded in xenon clusters.

We expand the time dependent electronic wave function of the polyatomic system, $\Psi(t)$, in terms of a canonical set of valence bond (VB) adiabatic state wave functions, $\phi_k(t)$,

$$\Psi(t) = \sum_k a_k(t)\phi_k(t) \tag{2.6}$$

and we write the VB wave functions $\phi_k(t)$ in terms of diabatic polyatomic basis functions (pbf's), Φ_j,

$$\phi_k(t) = \sum_j \Gamma_{kj}\Phi_j, \tag{2.7}$$

where the expansion coefficients Γ_{kj} are the DIIS eigenvectors. The pbf's, written as linear combinations of simple products of atomic functions (spaf's), are products of atomic and diatomic functions and are assumed to be eigenfunctions of their respective atomic and diatomic Hamiltonians with eigenvalues equal to experimental energies. The argon atoms and I^- ions are restricted to be in their ground states and we represent them by single $^1S_0$ functions since they have S symmetry closed shells. The I atoms as well as I^+ cations have P-symmetry open shells and are represented with ^2P and ^3P functions, respectively.

The diabatic polyatomic basis functions Φ_j are written as antisymmetrized products of S-symmetrical functions of the N argon atoms and $\zeta^{(j)}$ group functions of the iodine molecule,

$$\Phi_j = \hat{A}\zeta^{(j)}\prod_{i=1}^{N} |s^{(i)}\rangle, \tag{2.8}$$

where the index j indicates the electronic state of I_2. The zero overlap of atomic orbitals approximation (ZOAO), allows us to omit the antisymmetrization operator, $\hat{A}$ rendering the polyatomic wave function as a simple product of atomic and diatomic group functions. The error arising from this approximation is proportional to the square of the overlap

TABLE I. Molecular orbitals of I^-I^+.

Case c type	Case c type wave function	R_e(Å)	T_e (cm^{-1})	ω_e (cm^{-1})	$\omega_e\chi_e$ (cm^{-1})	Refs.
$D',(2_g)$	$1/\sqrt{2}\{\lvert 22\rangle\lvert S\rangle-\lvert S\rangle\lvert 22\rangle\}$ $1/\sqrt{2}\{\lvert 2-2\rangle\lvert S\rangle-\lvert S\rangle\lvert 2-2\rangle\}$	3.58	40 388.3	104.0	0.2065	59,60
$\beta,(1_g)$	$1/\sqrt{2}\{\lvert 21\rangle\lvert S\rangle-\lvert S\rangle\lvert 21\rangle\}$ $1/\sqrt{2}\{\lvert 2-1\rangle\lvert S\rangle-\lvert S\rangle\lvert 2-1\rangle\}$	3.61	40 821.0	105.0	0.2300	61,60
$D,(0_u^+)$	$1/\sqrt{2}\{\lvert 20\rangle\lvert S\rangle+\lvert S\rangle\lvert 20\rangle\}$	3.58	41 026.5	95.0	0.1400	62,60,57,58
$E,(0_g^+)$	$1/\sqrt{2}\{\lvert 20\rangle\lvert S\rangle-\lvert S\rangle\lvert 20\rangle\}$	3.65	41 412.0	101.4	0.2048	63,61,60
$\gamma,(1_u)$	$1/\sqrt{2}\{\lvert 21\rangle\lvert S\rangle+\lvert S\rangle\lvert 21\rangle\}$ $1/\sqrt{2}\{\lvert 2-1\rangle\lvert S\rangle+\lvert S\rangle\lvert 2-1\rangle\}$	3.67	41 621.0	95.0	0.2220	64,60
$\delta,(2_u)$	$1/\sqrt{2}\{\lvert 22\rangle\lvert S\rangle+\lvert S\rangle\lvert 22\rangle\}$ $1/\sqrt{2}\{\lvert 2-2\rangle\lvert S\rangle+\lvert S\rangle\lvert 2-2\rangle\}$	3.77	41 789.0	100.2	0.1300	64,60
$f,(0_g^+)$	$1/\sqrt{2}\{\lvert 10\rangle\lvert S\rangle-\lvert S\rangle\lvert 10\rangle\}$	3.57	47 026.0	104.2	0.2100	65,60
$g,(0_g^-)$	$1/\sqrt{2}\{\lvert 00\rangle\lvert S\rangle-\lvert S\rangle\lvert 00\rangle\}$	3.61	47 070.0	105.7	0.5000	60
$F,(0_u^+)$	$1/\sqrt{2}\{\lvert 10\rangle\lvert S\rangle+\lvert S\rangle\lvert 10\rangle\}$	3.59	47 218.0	96.0	0.3600	60
$G,(1_g)$	$1/2\{\lvert 11\rangle\lvert S\rangle-\lvert S\rangle\lvert 11\rangle\}$ $1/2\{\lvert 1-1\rangle\lvert S\rangle-\lvert S\rangle\lvert 1-1\rangle\}$	3.53	47 559.0	106.6	0.2151	66,60
(0_u^-)	$1/\sqrt{2}\{\lvert 00\rangle\lvert S\rangle+\lvert S\rangle\lvert 00\rangle\}$	3.79	50 100.0	99.4	(0.2000)	60
(1_u)	$1/2\{\lvert 11\rangle\lvert S\rangle+\lvert S\rangle\lvert 11\rangle\}$ $1/2\{\lvert 1-1\rangle\lvert S\rangle+\lvert S\rangle\lvert 1-1\rangle\}$	3.69	50 150.0	102.6	(0.2000)	60

integrals and has been shown to be small in DIM calculations on halogen atoms in noble gases.[34]

In principle we could include configurations that are neutral $Ar_n I_2$ as well as ion pair configurations, $Ar_n I^+I^-$ and charge transfer to solvent ionic configurations $Ar_{n-1}Ar^+I_2^-$, and take into account the couplings between these configurations. However, in our implementation of the method we neglect configurations that involve the positive charge delocalization in the matrix. The difference of the ionization energies of the Ar and I atoms suggests that the $Ar_{n-1}Ar^+I_2^-$ states will lie ~5 eV above any of the ion pair states of spectroscopic interest. Furthermore, we neglect the couplings between covalent and ionic configurations. This latter approximation, which is justified by the fact that for an I atom the ionization energy is much higher than its electron affinity so the ion pair states have much higher energies than any of the covalent states considered in our calculations, block-diagonalizes the Hamiltonian matrix into covalent and ionic configurations. As discussed above the charge transfer to solvent states is higher in energy again and so is completely decoupled from our calculations. In Fig. 5 where we present our calculated electronic states for I_2 in the argon matrix we see that the ion pair states are indeed well separated from the covalent states for this system.

Covalent valence states are calculated according to the methods detailed in Ref. 1 including in our basis set for the iodine molecule the 23 covalent electronic states that correlate with the ground term (^2P) iodine atoms, ten of which arise from $^2P_{3/2}+{}^2P_{3/2}$ (3/2,3/2), ten from $^2P_{3/2}+{}^2P_{1/2}$ (3/2,1/2), and three from $^2P_{1/2}+{}^2P_{1/2}$ (1/2,1/2) dissociation limits.[53]

Gas phase potential surfaces for the ion pair states have been the subject of much experimental investigation (see references in Table I as well as Refs. 54–58). For our calcula-

tion of ionic states, the basis set is now extended to include 12 ion pair states arising from the $I^-(^1S)+I^+(^3P)$ configurations, which group in six states $(0_g^+,0_u^+,1_g,1_u,2_g,2_u)$ that correspond to $I^+(^3P_2)$ and six states $(0_g^+,0_u^+,0_g^-,0_u^+,1_g,1_u)$ associated with $I^+(^3P_{1,0})$. These ion pair states are presented in Table I distributed in two blocks according to their different dissociation limits and classified according to their different symmetry species. In the first column of Table I we identify electronic states according to the value of the projection of the total angular momentum in the direction of the bond Ω and in the second column we summarize expressions for the diatomic wave functions $\zeta^{(j)}$. Any of these functions may be expressed by the linear combination that follows:

$$\zeta^{(j)}=c_1\lvert J_j^{(a)}M_j^{(a)}\rangle\lvert S^{(b)}\rangle+c_2\lvert S^{(a)}\rangle\lvert J_j^{(b)}M_j^{(b)}\rangle, \qquad (2.9)$$

where the ion pair electronic state of the I_2 molecule is labeled by index j and the labels (a) and (b) indicate the different iodine atoms. The ion pair molecular states are thus written in a basis set of simple products of atomic functions (spaf's) in which the closed shell I^- ion is modeled using a ^1S function and the I^+ ion is modelled using ^3P functions. These spaf's $\psi_{m,n}$ are thus defined as

$$\psi_{m,n}=\lvert S\rangle\lvert J^{(n)}M^{(n)}\rangle \quad J^{(n)}=2,1,0$$
$$M^{(n)}=-J^{(n)},-J^{(n)}+1,\ldots,J^{(n)}, \qquad (2.10)$$

where m enumerates the different $\lvert J^{(n)}M^{(n)}\rangle$ states listed above of cation n, in the total angular momentum representation (coupled representation), $\mathbf{J}=\mathbf{L}+\mathbf{S}$ and M is the projection of $\mathbf{J}$ in the direction of the bond. In this model of the ion pair states the other iodine particle is an anion with a spherical closed shell $\lvert S\rangle$ electronic charge distribution.
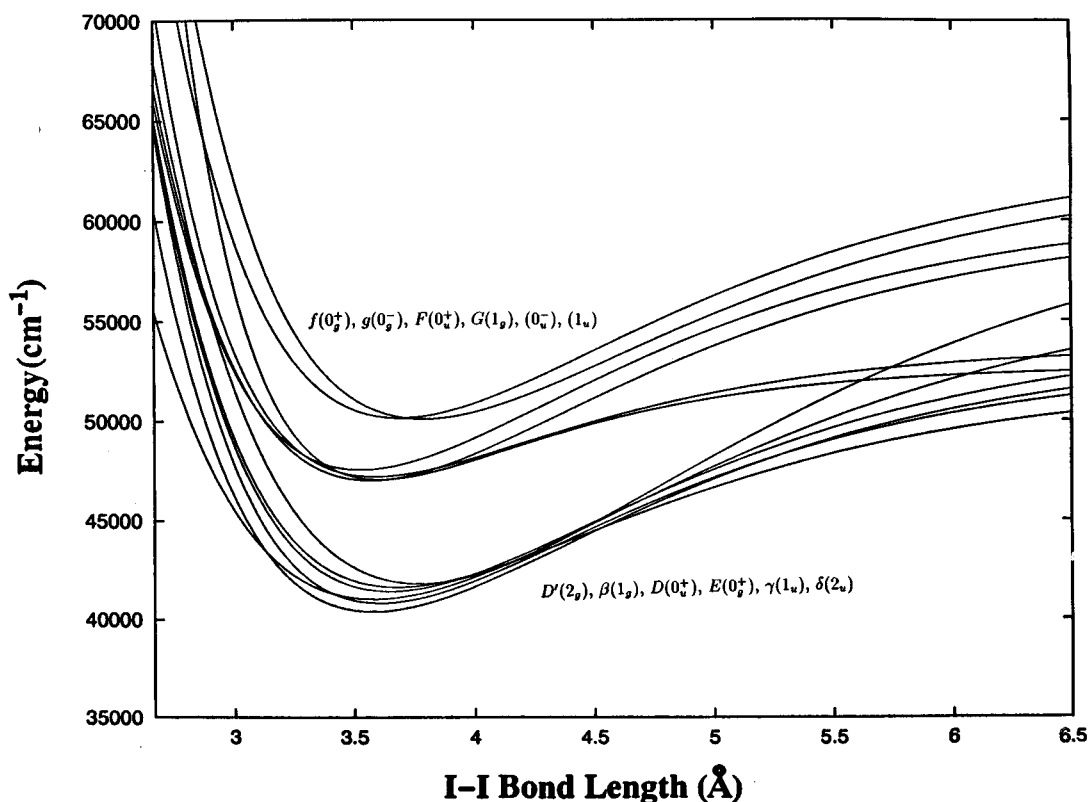
FIG. 1. Experimental gas phase potential surfaces for I^+–I^-. The six lowest and six highest states are labelled in order of increasing minimum potential value T_e as presented in Table I.

States with Ω different from zero are double degenerate. Each degenerate state corresponds to one of the two possible orientations for the projection of the total angular momentum in the direction of the bond. Consequently the 12 Hund's case (c) molecular states form a basis set of 18 states including degeneracies.

The energy levels of the system are now obtained in the usual way by forming the Hamiltonian matrix of order 18×18 with the basis set described above and diagonalizing.

Due to the lack of interatomic (atomic-diatomic) electron permutations in the polyatomic functions [ZOAO version of Eq. (2.8)], the Hamiltonian of the system can be partitioned into interatomic and atomic terms according to[67]

$$\hat{H} = \sum_K \sum_{L>K} H^{(KL)} - n \sum_K H^{(K)}, \qquad (2.11)$$

where $H^{(K)}$ is the Hamiltonian operator of atom K and contains all kinetic energy operators and intra-atomic potential energy terms that depend solely on the position of atom K and on the coordinates of those electrons initially assigned to this atom. Similarly, $H^{(KL)}$ is the Hamiltonian operator appropriate for the diatomic fragment KL.

The diatomic fragment Hamiltonian for I^-I^+, $H^{I^{(q_1)}I^{(q_2)}}$, is constructed from curves of pair potentials of states listed in Table I, that are presented in Fig. 1 and approximated by gas phase Morse functions

$$V = T_e + \frac{\omega_e}{4\chi_e}\{1 - \exp[-\sqrt{\omega_e \chi_e 4\pi c \mu/\hbar}(R - R_e)]\}^2, \qquad (2.12)$$

where μ is the reduced mass of the diatomic molecule and parameters R_e, T_e, ω_e, and $\omega_e\chi_e$, presented in columns 3–6, were taken from Refs. presented in column 7. Alternative forms for these interactions have been proposed[68,69] but due to the availability of parameters for the Morse potential given above we have used this form to describe all $I^- - I^+$ interactions.

The Morse parameters for the gas phase ion pair potential surfaces presented in Table I were obtained by fitting to many vibrational bands in the emission spectrum of the excited ion pair states.[60] These fitted forms are only reliable in the region of the excited ion pair state wells between ~3 and ~4.5 Å. One could imagine constraining the parameters during the fitting of these shifted Morse forms to take account of the fact that the different groups of states have common dissociation limits, however, such a constrained fit was not undertaken.[60] The added flexibility of the unconstrained fit probably gives curves which very accurately represent the well regions, but the behavior at large bond lengths, as seen in Fig. 1, does not reflect the correct pattern of common dissociation energies. As we shall see later (see discussion of

Figs. 4 and 5, for example), the position of the active probe absorption windows in these experiments lie in the range 3 to 4.5 Å and this is precisely the region where these unconstrained fitted curves are probably quite reliable.

The ArI^+ pair interactions were modeled by a potential constructed with a short range interaction term supplemented by a long range attraction which is dominated by a $-1/r^4$ term with significant contribution from a $-1/r^6$ term. The short range term is approximated by $Ar-I$ potentials of the usual Σ, Π, and $\bar{\Pi}$ orientations as described in Ref. 70. These potentials are constructed using the Morse-Morse-switching function-van der Waals (MMSV) potential forms from Ref. 71 for the $X1/2$, $I3/2$, and $II1/2$ potentials. The $X1/2$ and $I3/2$ states correlate with the $^2P_{3/2}+{}^1S_0$ asymptote, while the $II1/2$ correlates with $^2P_{1/2}+{}^1S_0$. 1/2 and 3/2 following X, I, and II are the Ω quantum numbers where Ω is the projection of the total electronic angular momentum along the molecular axis. In this article we follow the convention presented in our previous work[1] where vector Σ is in the reference frame of the diatomic fragment oriented along the $\mathbf{R}_{ij}$ vector, Π is perpendicular to Σ and located in the plane formed by $\mathbf{R}_{ij}$ and the x-axis, while $\bar{\Pi}$ is perpendicular to this plane (see Fig. 2 of Ref. 1). The Hamiltonian $H^{I^+Ar^{(i)}}$ is thus written in the reference frame of the diatomic fragment $I^+Ar^{(i)}$ as,

$$H^{I^+Ar^{(i)}} = \begin{bmatrix} V_\Pi & 0 & 0 \\ 0 & V_{\bar{\Pi}} & 0 \\ 0 & 0 & V_\Sigma \end{bmatrix}. \quad (2.13)$$

In order to express this Hamiltonian in the basis set of Eq. (2.10) we first transform it from the p states defined in the reference frame of the diatomic fragment, $(p_\Pi, p_{\bar{\Pi}}, p_\Sigma)$, to the fixed reference frame of the laboratory (p_x, p_y, p_z) according to the transformation

$$DH^{I^+Ar^{(i)}}D^{-1}, \quad (2.14)$$

where D is the Cartesian rotation matrix with row vectors constructed from the projections of the unit vectors $\hat{x}$, $\hat{y}$, and $\hat{z}$ along the Π, $\bar{\Pi}$, and Σ axes (see Fig. 2 of Ref. 1):

$$D = \begin{bmatrix} \sin(\alpha) & 0 & \cos(\alpha) \\ -\cos(\beta)\cos(\alpha) & \sin(\beta) & \cos(\beta)\sin(\alpha) \\ -\sin(\beta)\cos(\alpha) & -\cos(\beta) & \sin(\beta)\sin(\alpha) \end{bmatrix}. \quad (2.15)$$

The Hamiltonian $H^{I^+Ar^{(i)}}$ expressed in the basis set of p states defined in the fixed reference frame of the laboratory (p_x, p_y, p_z) is then transformed to the p basis functions defined in the reference frame of the iodine molecule according to the transformation defined by Eq. (2.14) where the new transformation matrix D is defined as the inverse of the Cartesian rotation matrix presented above, where now the bond vector connecting the atoms $I^{(1)}$ and $I^{(2)}$ defines the z-axis of the coordinate system.

This Hamiltonian, $H^{I^+Ar^{(i)}}$, is then transformed to the complex p basis functions, (p_1, p_0, p_{-1}), defined by

$$p_1 = [p_x + ip_y]/\sqrt{2}, \quad p_0 = p_z, \quad \text{and} \quad p_{-1} = [p_x - ip_y]/\sqrt{2} \quad (2.16)$$

according to the transformation defined by Eq. (2.14) where this next transformation matrix D is defined as follows:

$$D = \begin{bmatrix} 1/\sqrt{2} & i/\sqrt{2} & 0 \\ 0 & 0 & 1 \\ 1/\sqrt{2} & -i/\sqrt{2} & 0 \end{bmatrix}. \quad (2.17)$$

$H^{I^+Ar^{(i)}}$ is now a 3×3 matrix in the complex $|m_l\rangle$ basis set. In order to express it in the 9×9 uncoupled representation, $|m_l\, m_s\rangle$, we must perform the outer product with the 3×3 identity matrix, $\hat{\mathbf{1}}_3$, according to

$$H \otimes \hat{\mathbf{1}}_3 = \begin{bmatrix} H_{11} & 0 & 0 & H_{12} & 0 & 0 & H_{13} & 0 & 0 \\ 0 & H_{11} & 0 & 0 & H_{12} & 0 & 0 & H_{13} & 0 \\ 0 & 0 & H_{11} & 0 & 0 & H_{12} & 0 & 0 & H_{13} \\ H_{21} & 0 & 0 & H_{22} & 0 & 0 & H_{23} & 0 & 0 \\ 0 & H_{21} & 0 & 0 & H_{22} & 0 & 0 & H_{23} & 0 \\ 0 & 0 & H_{21} & 0 & 0 & H_{22} & 0 & 0 & H_{23} \\ H_{31} & 0 & 0 & H_{32} & 0 & 0 & H_{33} & 0 & 0 \\ 0 & H_{31} & 0 & 0 & H_{32} & 0 & 0 & H_{33} & 0 \\ 0 & 0 & H_{31} & 0 & 0 & H_{32} & 0 & 0 & H_{33} \end{bmatrix}. \quad (2.18)$$

Finally, the Hamiltonian is expressed in the coupled representation, $|JM\rangle$, according to the transformation defined by Eq. (2.14), where D is the Clebsh–Gordon matrix defined in the transformation expression

$$
\begin{array}{ccc}
|m_l m_s\rangle & = & D \qquad\qquad |JM\rangle
\end{array}
$$

$$
\begin{bmatrix}
|1 \;\; 1\rangle \\
|1 \;\; 0\rangle \\
|1 \;\; -1\rangle \\
|0 \;\; 1\rangle \\
|0 \;\; 0\rangle \\
|0 \;\; -1\rangle \\
|-1 \;\; 1\rangle \\
|-1 \;\; 0\rangle \\
|-1 \;\; -1\rangle
\end{bmatrix}
=
\begin{bmatrix}
1 & 0 & 0 & 0 & 0 & 0 & 0 & 0 & 0 \\
0 & \frac{1}{\sqrt{2}} & 0 & 0 & 0 & \frac{1}{\sqrt{2}} & 0 & 0 & 0 \\
0 & 0 & \frac{1}{\sqrt{6}} & 0 & 0 & 0 & \frac{1}{\sqrt{2}} & 0 & \frac{1}{\sqrt{3}} \\
0 & \frac{1}{\sqrt{2}} & 0 & 0 & 0 & \frac{-1}{\sqrt{2}} & 0 & 0 & 0 \\
0 & 0 & \frac{2}{\sqrt{3}} & 0 & 0 & 0 & 0 & 0 & \frac{-1}{\sqrt{3}} \\
0 & 0 & 0 & \frac{1}{\sqrt{2}} & 0 & 0 & 0 & \frac{1}{\sqrt{2}} & 0 \\
0 & 0 & \frac{1}{\sqrt{6}} & 0 & 0 & 0 & \frac{-1}{\sqrt{2}} & 0 & \frac{1}{\sqrt{3}} \\
0 & 0 & 0 & \frac{1}{\sqrt{2}} & 0 & 0 & 0 & \frac{-1}{\sqrt{2}} & 0 \\
0 & 0 & 0 & 0 & 1 & 0 & 0 & 0 & 0
\end{bmatrix}
\begin{bmatrix}
|2 \;\; 2\rangle \\
|2 \;\; 1\rangle \\
|2 \;\; 0\rangle \\
|2 \;\; -1\rangle \\
|2 \;\; -2\rangle \\
|1 \;\; 1\rangle \\
|1 \;\; 0\rangle \\
|1 \;\; -1\rangle \\
|0 \;\; 0\rangle
\end{bmatrix}
\tag{2.19}
$$

$Ar-I^-$ interactions are modeled by a MMSV empirical potential[71] and rare gas atom interactions are approximated by a Lennard–Jones potential with $\epsilon = 83.26$ cm^{-1} and $\sigma = 3.405$ Å.

The total Hamiltonian is then written as the direct sum over all diatomic-fragment Hamiltonians of the system as follows:

$$
H = H^{(I^- I^+)} + \hat{\mathbf{1}}_2 \otimes \left[\sum_{k=1}^{N} H^{I^+_{(a)} Ar^{(k)}} + \hat{\mathbf{1}}_9 \otimes \sum_{k=1}^{N} V^{I^-_{(b)} Ar^{(k)}} \right]
$$
$$
+ \left[\sum_{k=1}^{N} H^{I^+_{(b)} Ar^{(k)}} + \hat{\mathbf{1}}_9 \otimes \sum_{k=1}^{N} V^{I^-_{(a)} Ar^{(k)}} \right] \otimes \hat{\mathbf{1}}_2 + \hat{\mathbf{1}}_{18}
$$
$$
\otimes \sum_{i=1}^{N-1} \sum_{k>i}^{N} V^{Ar^{(i)} Ar^{(k)}},
\tag{2.20}
$$

where the constant monoatomic contribution appearing in Eq. (2.11) is omitted. The energy of the system is calculated relative to the energy of infinitely separated neutral species in the ground state:

$$
E_\infty = 2 E_{I[^2P_{3/2}]} + \sum_{j=1}^{N} E_{Ar}.
\tag{2.21}
$$

As presented above, the diatomic terms $H^{(ArI^-)}$, $H^{(ArI^+)}$ include the energy of polarization of neutral Ar atoms by the charged species I^- and I^+. However, in order to take account of the self-consistent many-body nature of the

electric field responsible for polarization we determine the induction energy in the electrostatic approximation separating it as a special term η_n,

$$
H_{mn,mn} = \langle \psi_{m,n} | \hat{H} | \psi_{m,n} \rangle = \sum_{i} \sum_{j>i} V_{Ar^{(i)} Ar^{(j)}}
$$
$$
+ \sum_{j} [\widetilde{V}_{I^+_n Ar_j} + \widetilde{V}_{I^- Ar_j}]
$$
$$
+ V_{I^+_{J^{(n)} M^{(n)}} I^-} + \eta_n
\tag{2.22}
$$

and we approximate η_n by the classical expression for the energy of polarization as follows[72–74]

$$
\eta_n = \sum_{j} \mu_j \left[\frac{\mathbf{R}_{jI^-}}{R_{jI^-}^3} - \frac{\mathbf{R}_{jI^+}}{R_{jI^+}^3} \right] + \sum_{j} \sum_{i>j} \mu_j \cdot \mathbf{T}_{ij} \cdot \mu_i
$$
$$
+ \sum_{j} \frac{\mu_j \times \mu_j}{2\alpha_j}.
\tag{2.23}
$$

In Eq. (2.22), $\widetilde{V}$ is defined as

$$
\widetilde{V} = V + \frac{C_4}{R^4},
\tag{2.24}
$$

where C_4 is expressed in terms of the atomic polarizability of Ar, α, and the charge of the ion q as

$$C_4 = \tfrac{1}{2}q^2\alpha. \qquad (2.25)$$

For the calculation of η_n we consider atoms as nonoverlapping polarizable spheres and compute the induced dipole moments μ_j self-consistently according to the following equation:

$$\mu_k = \alpha_k \left[\frac{\mathbf{R}_{kI^+} S(|R_{kI^+}|)}{R_{kI^+}^3} - \frac{\mathbf{R}_{kI^-} S(|R_{kI^-}|)}{R_{kI^-}^3} \right.$$
$$\left. - \sum_{j \neq k} \mathbf{T}_{jk} \cdot \mu_j \right], \qquad (2.26)$$

where $\mathbf{T}_{jk}$ are the components of the dipole-dipole interaction tensor given by

$$T_{jk} = -\frac{3}{r^5}\begin{bmatrix} x^2 - r^2/3 & xy & xz \\ xy & y^2 - r^2/3 & yz \\ xz & yz & z^2 - r^2/3 \end{bmatrix}, \qquad (2.27)$$

where r is the interatomic distance with cartesian components x, y, and z, and the switching function $S(R)$ is defined as[75]

$$S(R) = \begin{cases} 1.0 & \text{if } R < (r_C - r_S) \\ 1.0 + R^3(-6.0R^2 + 15.0R - 10.0) \\ \quad \text{if } (r_C - r_S) < R < r_C \\ 0.0 & \text{if } R > r_C \end{cases}, \qquad (2.28)$$

where r_C is equal to half of the length of the cell and $r_S = 1$ Å.

D. Calculation of transition dipole operator matrix elements

The $\mathbf{R}$-dependent electronic transition dipole operator matrix elements μ_{if}^{ad} between (VB) adiabatic states ϕ_j needed in the computation of the signals outlined in Sec. II B can be written in terms of the dipole operator matrix elements in the diabatic basis set, Φ_k, as follows

$$\mu_{fj_k}^{ad} = \langle \phi_f | \hat{\mu} | \phi_{j_k} \rangle = \sum_m \sum_n \Gamma_{mf}^* \Gamma_{nj_k} \langle \Phi_m | \hat{\mu} | \Phi_n \rangle, \quad (2.29)$$

where the pbf's, Φ_k, are linear combinations of products of atomic functions which are not explicitly specified within the DIM or DIIS formulation. Thus integrals of these functions over electronic coordinates r like the diabatic dipole operator matrix elements $\mu_{mn}^{di}(\mathbf{R}) = \langle \Phi_m | \hat{\mu} | \Phi_n \rangle (\mathbf{R})$ needed in Eq. (2.29) are not readily available. We have overcome this problem by assuming that the gas phase selection rules still operate for the diabatic transition dipole matrix elements. According to these selections rules, the diabatic transition dipole matrix elements are different from zero only for transitions between g and u states for which $\Delta\Omega = 0, \pm 1$ with Ω being the quantum number for the projection of the electronic angular momentum onto the I$-$I bond axis. Despite the fact that the $\Delta\Omega = \pm 1$ transitions are technically allowed, their intensities in the gas phase are typically at least 100 times smaller than those of the $\Delta\Omega = 0$ bands.[53,59,76] Thus in our calculations of the absorption intensities we have

included only transitions between diabatic states for which $\Delta\Omega = 0$. The final aspect of the selection rules for transitions between electronic states in the coupled Hund case (c) representation is that if $\Omega = 0$ the only allowed transitions are those which involve states with the same reflection symmetry in a plane containing the bond. Thus transitions $0^+ \leftrightarrow 0^+$ and $0^- \leftrightarrow 0^-$ are allowed while $0^+ \leftrightarrow 0^-$ is forbidden. Note that these symmetry considerations are for the total spin-orbit coupled wave functions in this representation.

The angular momentum projection quantum numbers and symmetries in the coupled representation are given in parentheses in the state labels of the diabatic basis functions used to describe our DIIS ion pair states presented in Table I. The adiabatic states occupied by our excited nonadiabatic MD trajectories will be linear combinations of diabatic basis states predominately in the covalent state manifold which dissociates to two $J = 3/2$ atoms [the (3/2,3/2) covalent manifold], or the initially excited B state from the (3/2,1/2) covalent manifold. The covalent diabatic states we thus consider in our intensity calculations have the following symmetry labels presented in the uncoupled representation, followed by the coupled representation in parentheses:[1] $X, {}^1\Sigma_g^+(0_g^+)$, $A', {}^3\Pi_{2u}(2_u)$, $A, {}^3\Pi_{1u}^+(1_u)$, ${}^3\Pi_u(0_u^-)$, $B, {}^3\Pi_u(0_u^+)$, ${}^1\Pi_u(1_u)$, ${}^3\Pi_{2g}(2_g)$, $a, {}^3\Pi_{1g}(1_g)$, $a', {}^3\Sigma_g^-(0_g^+)$, ${}^3\Sigma_u^+(0_u^-)$, and ${}^3\Delta_{3u}(3_u)$.

Using the selection rules for transitions between states in the coupled representation outlined earlier, together with the diabatic state symmetry designations listed above and in Table I, we have calculated adiabatic transition dipole moment matrix elements according to Eq. (2.29) and included in our calculations all the following allowed transitions between diabatic states

[Type (i) transitions:] $X(0_g^+) \leftrightarrow D(0_u^+)$, $X(0_g^+) \leftrightarrow F(0_u^+)$, $A'(2_u) \leftrightarrow D'(2_g)$, $A(1_u) \leftrightarrow \beta(1_g)$, $A(1_u) \leftrightarrow G(1_g)$,
[Type (ii) transitions:] ${}^3\Pi_u(0_u^-) \leftrightarrow g(0_g^-)$, ${}^1\Pi_u(1_u) \leftrightarrow \beta(1_g)$, ${}^1\Pi_u(1_u) \leftrightarrow G(1_g)$, ${}^3\Pi_{2g}(2_g) \leftrightarrow \delta(2_u)$, $a{}^3\Pi_{1g}(1_g) \leftrightarrow \gamma(1_u)$, $a{}^3\Pi_{1g}(1_g) \leftrightarrow (1_u)$, $a'{}^3\Sigma_g^-(0_g^+) \leftrightarrow D(0_u^+)$, $a'{}^3\Sigma_g^-(0_g^+) \leftrightarrow F(0_u^+)$, ${}^3\Sigma_u^+(0_u^-) \leftrightarrow g(0_g^-)$, and
[Type (iii) transitions:] $B{}^3\Pi_u(0_u^+) \leftrightarrow f(0_g^+)$, $B{}^3\Pi_u(0_u^+) \leftrightarrow E(0_g^+)$.

Here we have divided the transitions into three distinct groups; those originating from bound covalent states which dissociate to a pair of $J = 3/2$ atoms [type (i) transitions], transitions originating from unbound covalent states which dissociate to a pair of $J = 3/2$ atoms [type (ii) transitions], and transitions originating from the B state [type (iii) transitions] which form part of the covalent manifold of states which dissociate to a $J = 3/2$ atom and a $J = 1/2$ atom.

In our calculations we have further assumed that the electronic transition moments, $\mu_{mn}^{di}(\mathbf{R})$, are weakly dependent on solvent coordinates and depend only on the I$-$I bond length according to simple functional forms presented in the literature[58,77,78] that have been successfully investigated in studies and simulations of $D \to X$ and $E \to B$ fluorescence spectra of I_2 in the gas phase. For all type (i) transitions we assume the same dependence on bond length and the same

strength with the following expression for the dipole matrix element[78]

$$\mu_{(i)}^{di}(R_{I-I}) = A \, \exp[-R_{I-I}], \qquad (2.30)$$

with $A = 10$. The dipole matrix elements for all type (ii) transitions are assumed to have the same exponentially decaying bond length dependence but the strength of the dipole matrix elements coupling these dissociative states to the ion pair manifold are assumed to be smaller than the matrix elements for the bound states. Thus

$$\mu_{(ii)}^{di}(R_{I-I}) = B \, \exp(-R_{I-I}), \qquad (2.31)$$

with $B = 0.1$.

All transitions originating from the B state [our type (iii) transitions] have been modeled using the following form[77]

$$\mu_{(iii)}^{di}(R_{I-I}) = \frac{0.00285}{0.09 + (R_{I-I} - 3.89)^4}. \qquad (2.32)$$

This choice makes the type (iii) transitions about 100 times less intense than the type (i) transitions, consistent with experimental observations.[59,76] In the above expressions all bond lengths are in Ångstroms. The type (i) and (iii) functions used here are based on information from previous gas phase experiments, while the type (ii) dipole function is proposed by the authors. We found that our A state photoexcitation signals are insensitive to the choice of the type (ii) dipole function and these transitions could be made just as intense as the type (i) transitions with little effect on the A state photoexcitation signal. However, in order to obtain qualitative agreement with the experimental results for krypton presented in Fig. 1 of Ref. 45 we assumed that type (ii) transitions from the dissociative states were considerably less intense than the type (i) transitions. Thus we conclude that type (i) transitions make the most significant contribution for these signals.

III. RESULTS

We present our results in three subsections. First we compare our calculated pump-probe absorption signals for A state photoexcitation of I_2 in solid argon with the published experimental results of Apkarian and co-workers.[42] After demonstrating the accuracy of our calculations we use these methods to predict the pump-probe absorption signals for B state excitation of I_2 in this system. This higher energy excitation can open electronically nonadiabatic channels to predissociation which we have surveyed in our recent liquid phase studies.[1] Here we explore the effects of these predissociation channels on the ultrafast pump-probe spectroscopy of I_2 in solid argon and compare and contrast our findings with available experimental results and the behavior observed for lower energy A state excitation dynamics. Finally we explore the effects of changing the nature of solid matrix on the excited state relaxation dynamics by comparing the above results in argon matrices with A and B state relaxation dynamics in solid xenon.
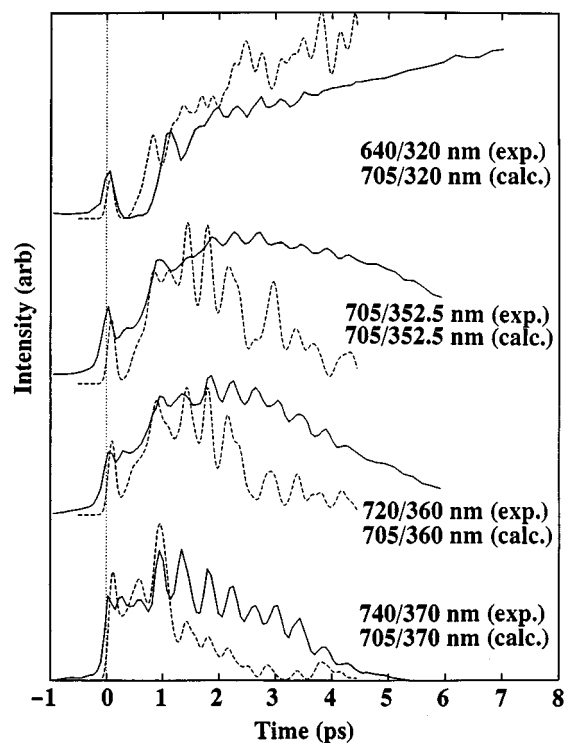

FIG. 2. Comparison of experimental (solid) and calculated (dashed) pump-probe signals for A state pump excitation of I_2 in solid argon at $T = 40$ K and $\rho^* = 1.07$. Results for a range of pump-probe wavelengths are presented.

A. Detailed comparison with available experimental results: A state excitation of I_2 in solid argon.

In order to check on the accuracy and reliability of our calculated signal we compare our results with the experimental pump-probe signals obtained by Apkarian and co-workers for A state excitation of I_2 in solid argon in Fig. 2. This figure shows the strong trends in these signals with probe wavelength. In the experiments the probe pulses are obtained by frequency doubling the pump. As discussed by Apkarian and co-workers changing the pump frequency shifts the relative timings of the different peaks in these signals by fairly small amounts due to the fact that the excited state packet is placed at only slightly different positions as the pump wavelength is changed. In our calculations we have fixed the pump wavelength at 705 nm, run our ensemble of nonadiabatic dynamical trajectories from this initial resonance condition, and then conducted the analysis of these nonadiabatic dynamical trajectories at various probe wavelengths as outlined in Sec. II B.

The first feature to note when comparing our calculated signals with the experimental results is that the overall shapes of the experimental data, and the trend in these shapes with probe wavelength is well reproduced by our calculations. At the longest wavelength ($\lambda_{probe} = 370$ nm) for example, the signals rise rapidly to the first peak at very short times, then show a plateau with some superimposed structure for about the first 1 ps, following which the signals again rise rapidly to their maximum values at around the 1 ps mark. The subsequent signals next show evidence of a coherent

vibrational feature which undergoes decay out to about 4–5 ps. Our calculated signal over this time interval decays faster than observed experimentally, but the frequency of the coherent vibrational feature is well reproduced.

At the shortest probe wavelengths (λ_{probe}=320 nm), on the other hand, the calculated and experimental signals again agree with one another quite accurately and show qualitatively different behavior from that observed at the longer wavelengths. The first major difference to note is that the structured plateau feature between 0 and 1 ps is now completely absent and the spectrum is nearly dark between the sharp peak near zero time and the reappearance of signal near t=1 ps. Following this sharp peak at ~1 ps the signals at this shortest wavelength continue to increase out beyond 5 ps. This is in marked contrast to the long time decay observed both experimentally and theoretically at the longer wavelengths discussed above.

The peak near t=1 ps in the experimental results for λ_{probe}=320 nm is delayed relative to the peak at zero time compared with our calculated results. This delay is most likely due to the fact that for this highest energy pump excitation the experimental wavepacket is placed higher on the repulsive A state wall initially so it makes excursions to larger bond extensions which delay the relative timings of the peaks. As mentioned above, in our calculations we have fixed the pump energy and varied the probe unlike the experimental situation where the pump and probe are both varied. The calculated and experimental timings for all the longer wavelengths are in better agreement because these packets are all placed lower on the repulsive wall for the longer wavelengths and the signals are thus reasonably well approximated by our constant probe excitation assumption.

At intermediate wavelengths the different features outlined above merge continuously from one extreme to the other; the feature between 0 and 1 ps gradually dying out as the wavelength is decreased, and the long time signal decay at longer wavelengths is slowly pushed out until we see only the increasing signal at the shortest wavelengths. The accuracy with which these trends and features in the experimental signals are reproduced by our calculations is remarkable given the crude nature of our assumed dipole moment functions, and the lack of any adjustable parameters in the covalent potential surfaces which determine the nonadiabatic dynamics or the ion pair surfaces which influence our calculated signals through the resonance condition.

In Fig. 3 we resolve our calculated signals into contributions from the transitions originating in the A, A', and other diabatic electronic states. From this break down of our calculated signals we see that over the 0–5 ps interval after photoexcitation to the A state, the probe signals at all wavelengths studied are dominated (~75%) by continued A state absorption, though there is an important contribution (~20%) from the close, lower lying A' state which appears very shortly after the initial A state excitation due to strong nonadiabatic mixing between these states. The A and A' contributions to the signals have similar coherent features but are initially out of phase with one another. These characteristics are most likely due to the fact that the difference
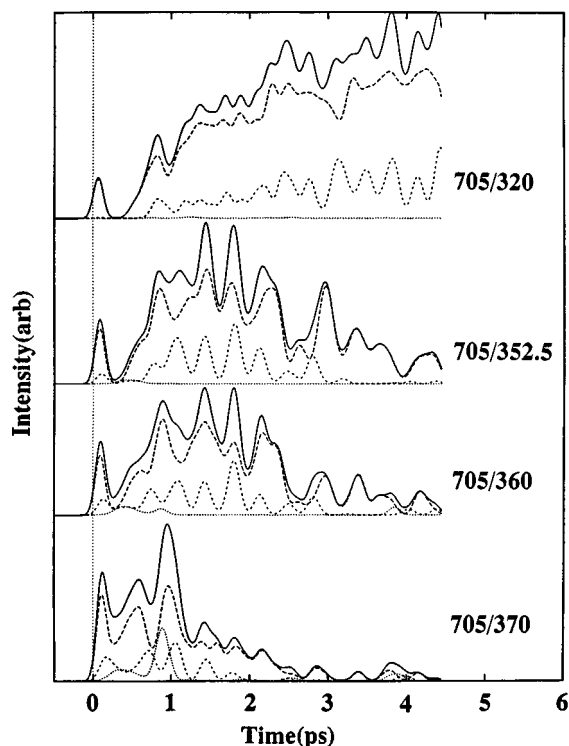

FIG. 3. Analysis of calculated pump-probe signals for A state pump excitation of I_2 in solid argon at T=40 K and ρ^*=1.07. Total signal (solid curve) is broken down into contributions from probe absorption transitions originating in the A state (long dashes), A' state absorption (short dashes), and probe absorptions originating from all other states in (3/2,3/2) covalent manifold (dots). Results for a range of pump-probe wavelengths are presented.

potentials ΔV_{fi} responsible for A and A' absorptions have similar shapes and that there is a delay time for relaxation of population from the A to the A' state. It is interesting to note that the A' state actually establishes a stable, slowly growing population over the entire time of simulation. Despite this, the signal contribution from the A' state initially grows in, then rapidly decays leaving only signal due to absorption from the A state at longer times. This rapid disappearance of A' signal occurs because trajectories on the A' surface rapidly move out of resonance with the probe, while A state trajectories stay resonant for longer. This rapid decrease of A' absorption is probably what is responsible for our total calculated signals decaying too quickly at longer times compared with experiments as seen in Fig. 2. It is likely that the upper D' state responsible for most of the A' absorption intensity moves out of resonance a little too rapidly as the bond vibration relaxes after excitation. The most questionable part of the D' surface we have used in these studies is the short range repulsive region. As we shall see later, this is the region of the upper D' state most relevant for $A' \leftrightarrow D'$ absorption when the ensemble of trajectories populating the A' state undergo vibrational relaxation. On the other hand, the β state which is responsible for most of the A state absorption, seems more reliable and we believe that at longer times the signals should actually have comparable contributions from both A and A' absorptions. The increased A'

absorption would make our total calculated signals decay slower, giving better agreement with experimental observations at longer wavelengths.

To understand the origin of the various features of the signals in Fig. 2, we plot the bondlength histories of all our ensemble members in Fig. 4. In this figure time goes up the y-axis and the x-axis gives the bond extension. These bondlength histories are determined by the nonadiabatic dynamics following the pump pulse, and where these trajectories go determines how the different wavelength probe pulses will be absorbed. Above these trajectories we have stacked traces of the signals at the various probe wavelenths computed along our trajectories. These probe signals are plotted as a function of the bondlength along our dynamical trajectories to show where the different probe pulses are absorbed. These upper panels thus give the average positions and shapes of the probe absorption windows, and the time history of passage of the trajectories through these windows gives rise to the dynamics of our calculated signals presented in Fig. 2.

The variation of the positions of these probe absorption windows displayed in the upper panels of Fig. 4 can be understood from the calculated covalent and ion pair state electronic energy levels displayed in Fig. 5. In this figure we present the state energies for I_2 in a perfect argon fcc crystal. The I_2 molecule is placed at the lowest energy equilibrium geometry and its bond length is stretched holding its orientation and center-of-mass fixed at its initial values. To understand how the resonance condition selects out the bondlength windows displayed in Fig. 4 we have overlayed Fig. 5 with a curve of the difference potential, ΔV_{fi} between the first excited adiabatic covalent state (which corresponds to the A' diabatic state for most important bondlengths) and the lowest energy adiabatic ion pair state (which corresponds to the D' diabatic state for most bondlengths). The probe resonance condition occurs when the horizontal probe energy values intersect this difference potential curve as well as any of the various other possible difference potentials. We see that for the highest probe energies (shortest λ_{probe}) the resonance condition is satisfied for both shorter bondlengths (around 3.2 Å), and longer bondlengths well beyond ~ 4 Å. For lower probe energies the two resonance windows move towards one another and begin to coalesce at the longest wavelengths used in these studies.

In Fig. 5 we also overlay the A and B state pump excitation energies. The approximate turning points of the classical motion occur when the occupied state potential curves (typically the lower energy covalent states at longer bondlengths) intersect these excitation energies. These resonance and turning point conditions for the fixed equilibrium center-of-mass position and orientation of the I_2 in the rigid lattice give only estimates of how far the trajectories go and where they will absorb or emit a photon. Our trajectories sample distorted and dynamically changing configurations of the system and so these equilibrium frozen lattice results serve only as a rough guide to what we should expect. From the signal traces presented in Fig. 4 we see that these estimates are very reasonable; the $\lambda_{probe}=320$ nm signal traces
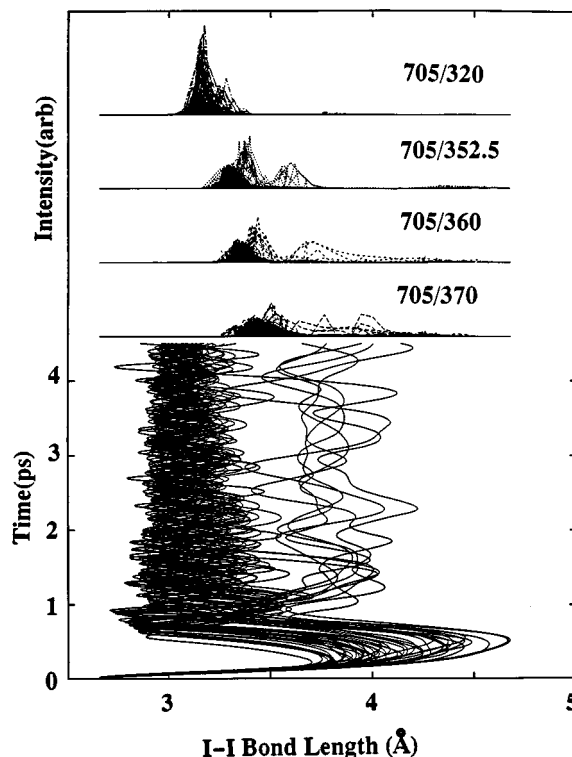

FIG. 4. Lower panel shows I–I bond length trajectories as functions of time following A state pump excitation of I_2 in solid argon at $T=40$ K and $\rho^*=1.07$. Upper panels show probe signals calculated along these trajectories plotted as functions of bond length. These plots show which bond lengths give strongest probe absorption signals and how these probe windows shift as the pump-probe wavelength is varied.

show a single main peak centered at around 3.2 Å, consistent with the bondlength at which our representative energy gap function in Fig. 5 is cut by the 320 nm probe energy. From this figure we further see that the outer resonance condition for $\lambda_{probe}=320$ nm is satisfied at beyond 5 Å. We do not see a peak in the signal traces at such bondlengths in Fig. 4 simply because none of our trajectories make it to this bond extension, which is consistent with having the turning point for the A state pump excitation ($\lambda_{pump}=705$ nm) just beyond 4.5 Å as it is presented in Fig. 5.

At progressively longer probe wavelengths ($\lambda_{probe}=352.5$, 360.0, and 370.0 nm) we see the inner resonance condition (Fig. 5) moves to longer bondlengths consistent with the motion of the dominant peak in the signal traces in Fig. 4. As discussed above the outer resonance condition in Fig. 5 shifts in with increased wavelength but it never moves in closer than about 4.2 Å. We only see strong contributions from this outer window absorption in the longest wavelength signal traces in Fig. 4.

From the bondlength trajectories we see that the excited state dynamics first takes the I_2 bond through the shortest bondlength windows at very early times giving rise to the first peaks in the calculated spectra in Fig. 3 very close to zero time. At around the 0.5 ps mark the trajectories go through the first turning points of their motion. Some do this
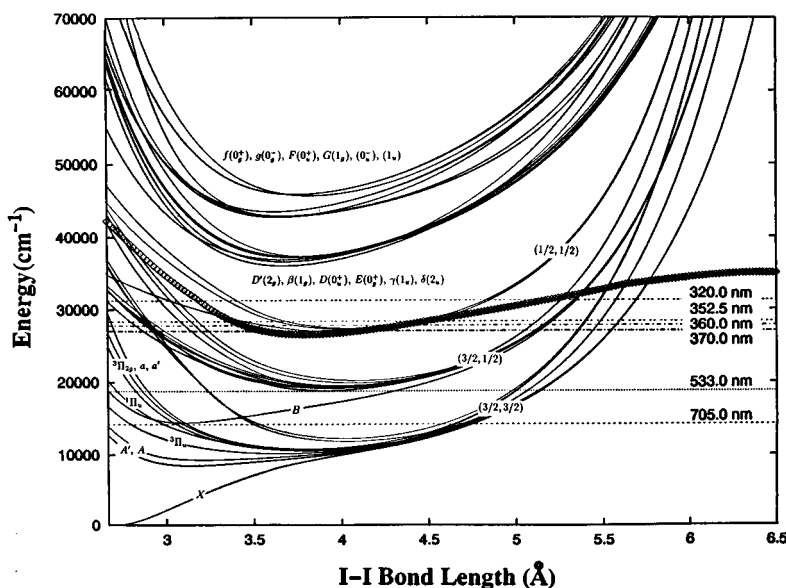
FIG. 5. Potential energy curves as a function of I–I bond length obtained from DIM calculations for covalent (lowest three groups of states) and ion pair (upper two groups) manifolds of I_2 positioned in its minimum energy orientation in a double substitutional cavity in a frozen argon matrix with $\rho^* = 1.07$. The ion pair states are labeled as in Fig. 1, and the three covalent manifolds are labeled according to their different total angular momentum dissociation products. Horizontal traces indicate experimental pump energies for A state ($\lambda_{pump} = 705$ nm) and B state ($\lambda_{pump} = 533$ nm) pumping. The bond lengths where these total energy traces intersect the potential curves for the states of the lowest covalent manifold, or the B state diabat, indicate the approximate turning points of the classical motion over these various surfaces. The curve labeled by diamond symbols gives an example of an adiabatic potential difference curve $\Delta E_{fi} = E_f^{ion} - E_i^{cov}$ (here $i = 2$, and $f = 1$). When this energy difference curve intersects the various probe energy traces ($\lambda_{probe} = 370 - 320$ nm) the probe resonance condition is achieved giving approximate bondlengths for the inner and outer probe resonance windows.

earlier and at shorter bondlengths while other trajectories undergo almost unperturbed motion until they encounter the repulsive solvent wall at beyond 4.5 Å extension. This dispersion results due to the different environments around the I_2 sampled as it tumbles about in the low temperature lattice at equilibrium on its ground state potential surface. For the 370 nm probe pulse from the bottom trace in Fig. 4 we see that many trajectories which make it to bond extensions beyond about 4 Å have the energy gap between their occupied state and the ion pair manifold resonant with this probe pulse and thus show contributions to the second window absorption. The motion through the outer window at this longest probe wavelength thus gives rise to the peak in the 370 nm probe signal at around 0.5 ps observed in Fig. 2. The fact that the relative intensity of this signal arising from passage through the outer window around the 0.5 ps mark agrees well with the experimental results indicates that the assumed functional form of the bondlength dependence of the diabatic dipole moment functions is reasonably reliable.

As we increase the probe pulse energy (lowering the wavelength to say $\lambda_{probe} = 320$ nm), we see that the inner most resonance window shifts to shorter bondlengths while the outer window will shift to longer bondlengths due to the curvature of the difference potentials between states in the ionic and covalent manifolds (see solid phase curves in Fig. 5). From Fig. 4 we see that our nonadiabatic trajectories do not reach the outer resonance window for the 320 nm probe pulse and consequently our calculated signals have a feature associated with passage through the outer resonance window that gradually disappears as the probe wavelength is de-

creased (see Fig. 3), almost quantitatively reproducing the trend observed in the experimental signals in Fig. 2.

The wavelength dependence of the longer time dynamical response observed in the experiments and reproduced qualitatively in our calculated signals (see Fig. 2), can also be understood from the trajectories and the variation of the window positions displayed in Fig. 4. The more rapidly decaying longer time behavior observed in our calculations at $\lambda_{probe} = 370$ nm arises because the inner most probe absorption window, centered at 3.4 Å, is positioned very close to the outer turning point of the A or A' state vibrational motion as we see from Fig. 4. As the A/A' state vibrational motion damps due to vibrational relaxation and dissipation to the solvent, the amplitude of the bond extensions decays, and the trajectories thus move out of the probe absorption window giving a decreasing signal at longer times. Thus the long time decay of the signal for $\lambda_{probe} = 370$ nm reflects this energy dissipation from the excited I_2 vibration.

From Fig. 4 we see that for $\lambda_{probe} = 320$ nm the probe absorption window is positioned slightly to the right of the A/A' state equilibrium bondlength, thus as the excited state vibrational motion dissipates energy and the amplitude of the bond extensions decays, trajectories spend more time in this inner probe window so we see the probe absorption signal increasing steadily with time. The fact that our calculations reproduce these variations in signal decay rate with probe wavelength reasonably well indicates that the DIM manybody excited electronic potentials are accurate functions of both intra- and intermolecular coordinates.

B. Predicted *B* state excitation of I$_2$ in solid argon

In this section we present our calculated signals at various probe wavelengths following pump excitation of I$_2$ at $\lambda_{pump} = 533$ nm to its B state in solid argon matrices. This excitation is expected to give qualitatively different dynamics from the A state excitation studies described in the previous section since the B state diabatic surface, being the lowest energy bound state from the excited (3/2,1/2) manifold, is crossed by several predissociative states from the (3/2,3/2) manifold in the bondlength range 3 Å $\leq R_{I-I} \leq$ 3.5 Å as we see in Fig. 5. In our previous work on B state photoexcitation of I$_2$ in liquid xenon[1] we showed that these diabatic curve crossings give rise to strong nonadiabatic effects which have a profound influence on the relaxation dynamics. In the A state excitation studies presented above we found that the probe signals were dominated by continued A state absorption, combined with some transient A' state signal which resulted from the nonadiabatic mixing between these two close lying states. Here we thus explore the influence on the expected pump-probe signals of a more energetic excitation in which the relaxation dynamics involves considerably more complicated nonadiabatic mixing between relaxation channels.

Fortunately these calculations do not tread on completely unknown ground just yet as Apkarian and co-workers have reported experimental pump-probe signals for B state photoexcitation of I$_2$ in solid krypton matrices.[45] In Fig. 6 we compare our calculated results for 533/363 and 533/368 nm pump-probe wavelengths in solid argon with their experimental 533/400 nm pump-probe signals in solid krypton. Our choice of probe wavelength is based on the fact that emission from ion-pair states occurs at 382 nm in Ar and 423 nm in Kr,[9] significantly shifted from its gas phase origin at 340 nm.[10] Our calculations of the ion pair states of I$_2$ in solid argon, reproduce this red shift remarkably well showing that it can be completely understood in terms of solvation of the ionic upper state in the polarizable matrix.

From Fig. 6 we see qualitative agreement between the signal decay and coherent structure in our calculated signals in argon and experimental results in krypton. The main difference between the calculated signals for I$_2$ in argon and the experimental signal in solid krypton seems to be the period of the coherent vibrational feature which sets in at about ~0.75 ps. Our calculations in argon show a slightly higher vibrational frequency than the experiments in krypton, which is probably due to the bigger double substitutional cavity for I$_2$ in the solid Kr matrix. In Fig. 7 we explore the influence of probe wavelength on our calculated signals and decompose them into contributions from different states. We see that there is a small feature in our calculated spectra close to zero time, in marked contrast to the strong features near zero time we saw in our calculated A state signals in Fig. 3.

The reason for this qualitative difference between early time signals for A and B state excitation is that the covalent states which are occupied during the early time nonadiabatic relaxation dynamics following B state excitation are either out of resonance with the appropriate ion pair states to which
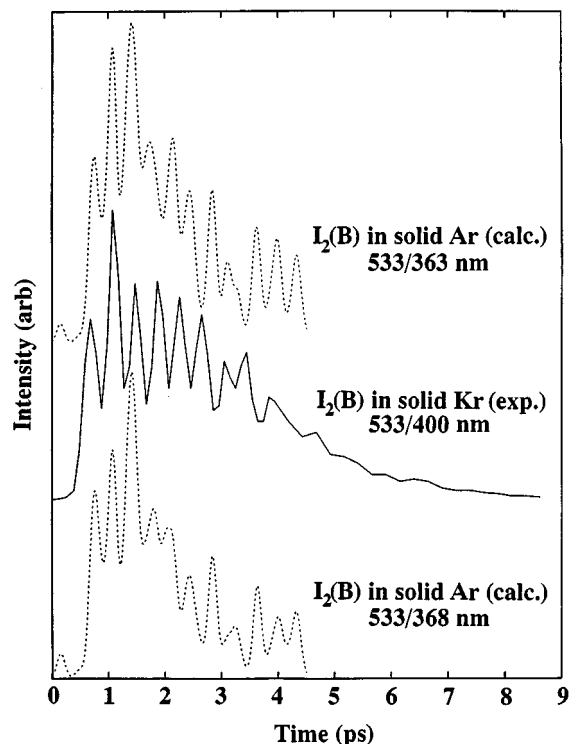

FIG. 6. Comparison of experimental pump-probe signals for B state excitation of I$_2$ in solid krypton (solid curve) and calculated signals for the same pump excitation in solid argon (dashed curve) at $T = 40$ K and $\rho^* = 1.07$. Results for two different probe wavelengths are presented in an effort to gauge the effect of differing solvent polarizability on ion pair state energy and probe wavelength.

they are dipole coupled, or the dipole oscillator strengths of the occupied states which are in resonance are small, resulting in very little probe absorption. The early time nonadiabatic relaxation dynamics following B state excitation in solid argon is very similar to the nonadiabatic dynamics we reported following B state excitation in liquid xenon. Some nonadiabatic dynamical trajectories exit the B state on the very first bond extension within 50–100 fs after excitation. These rapidly relaxing trajectories enter one of three possible major predissociative diabatic states which have strong solvent induced nonadiabatic coupling to the B state. These three predissociative channels occur via the $^1\Pi_u$, $^3\Pi_{2g}$, or a states. Within our model of the transition dipole matrix elements between the covalent and ion pair diabatic states summarized in Sec. II D the type (ii) transitions possible from these predissociative states all have relatively small oscillator strengths so despite the fact that they may be resonant they make little contribution to the calculated probe signals. The same is true for trajectories which behave diabatically and remain in the B state during their early time dynamics. The type (iii) transitions from the B state to the ion pair manifold may come into resonance with the probe pulse during this early time dynamics but our model for the dipole oscillator strength for these transitions makes these probe absorptions relatively weak as well.

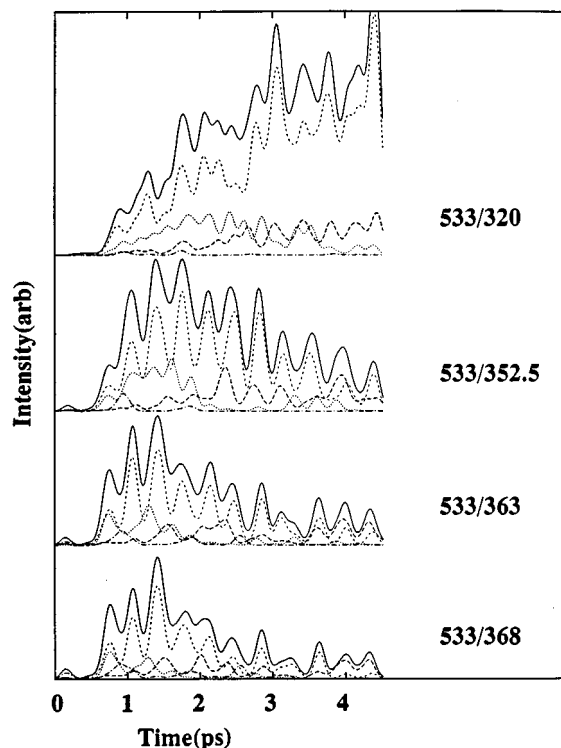There is some confusion in the experimental paper[45] concerning the precise specification of the time origin. The

FIG. 7. Analysis of calculated pump-probe signals for B state pump excitation of I_2 in solid argon at $T=40$ K and $\rho^*=1.07$. Total signal (solid curve) is broken down into contributions from probe absorption transitions originating in the A state (long dashes), A' state absorption (short dashes), X state absorption (dots), and probe absorptions originating from all other states in covalent manifold (dot-dash curve). Results for a range of pump-probe wavelengths are presented.

experimental data presented in Fig. 6 was taken directly from Fig. 1 of Ref. 45. Later in this same paper the time origin is arbitrarily shifted to the beginning of the first probe absorption peak and there is no discussion as to why this data is presented with two different time origins. The only way that this second time origin, with virtually no delay between pump and probe pulses, could be rationalized within the nonadiabatic dynamics predicted by our calculations is if the type (iii) probe absorption transitions from the excited B state to the ion pair manifold were to be made considerably more intense, as these transitions are the only ones resonant with the probe at early times. This however is inconsistent with the relative intensities measured in the gas phase of the possible B and A state absorptions resonant with the probe. As soon as the A state starts to be appreciably populated by the nonadiabatic dynamics, absorptions from this state are roughly 100 times more intense than the probe resonant transitions possible from the B state so a strong A state signal is expected to grow in after the early time nonadiabatic transient dynamics consistent with the delayed appearance of probe absorption which we see in our calculations and is observed in the experimental results reported in Fig. 1 of Ref. 45.

In Fig. 8 we plot the bondlength histories and signal traces for our initial B state excitation studies, and comparing with the results we presented in Fig. 4 for our A state

excitation studies we find some significant qualitative differences. For about the first 0.5–0.75 ps we find that some trajectories remain in the B state and undergo more than two vibrational periods on this bound excited state surface. On each bond extension some of these B state trajectories bifurcate into the various predissociative states and they subsequently undergo extremely large bond extensions out to between 5 and 6 Å (beyond even the turning points indicated in the frozen lattice results in Fig. 5). The first wave of predissociating trajectories recombines at around the ~0.75 ps mark and they do so into the A, A', and X states. This is clear from the appearence of the thick group of trajectory traces which oscillate around an equilibrium position of about 3.2 Å as we saw before in Fig. 4 for the A and A' state recombinations. The additional group of trajectories which show very large amplitude and much higher frequency vibrations about an equilibrium position around 2.7 Å characterizes the new recombination channel into the X state which was not evident in our A state excitation studies. The recombination into these A, A', and X states at ~0.75 ps give rise to the onset of the strong probe absorptions resulting from the type (i) transitions coming into resonance between these occupied states and their ion pair partners as we see in Fig. 7.

From the break down of our calculated B state excitation signals presented in Fig. 7 we see that in addition to the new component absorption associated with trajectories recombining in the X state, the dominant contribution to the probe signal is no longer due to the A state as we found for A state pumping. For our B state studies, in contrast, we find that the probe signals are now dominated by absorption from the lower energy A' state. The new X state absorption appears as a transient feature lasting only out to about 2 ps at longer probe wavelengths, but stays in resonance with the probe for considerably longer at shorter probe wavelengths.

C. Comparison of A and B state excitation of I_2 in solid argon and xenon

In this final section we explore the influence of solvent on the dynamics following initial A and B state photoexcitation in different rare gas matrices. We thus compare the dynamics in argon reported in the earlier sections with results we find for xenon matrices.

In Fig. 9 we plot our calculated potential curves as a function of I_2 bondlength in the frozen xenon matrix. Comparing with our results in Fig. 5 for the argon matrix we see that the effect of the larger double substitutional solvent cavity in xenon gives energy surfaces which are almost flat and appear very much like the gas phase results out to around 4–5 Å (see Fig. 1 from Ref. 1) in marked contrast to the strongly curved surfaces we find for the tighter double substitional cavity in the argon lattice. In xenon the dense charge-transfer-to-solvent manifold associated with states involving delocalization of the positive charge to various p-like hole states on the xenon atoms of the form $I+I^-+Xe^+$ should lie above, but quite close to the ion pair manifold since the difference in the ionization potentials for I and Xe is only about 1.67 eV compared to the situation in
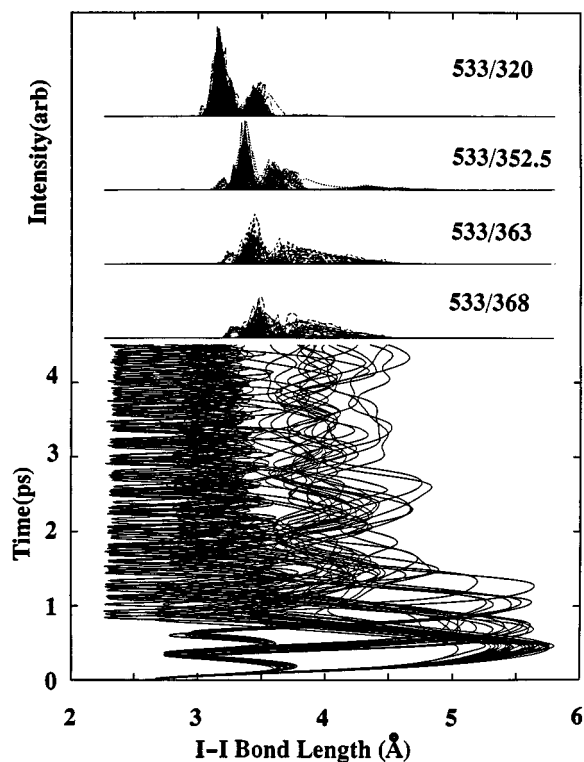
FIG. 8. Same as Fig. 4 only here results for B state excitation of I_2 in solid argon are presented.

argon where the ionization potential difference is ~ 5.3 eV. The possibility of overlap between the ion pair and charge transfer manifolds in xenon thus complicates the calculation of probe excitation signals in this solvent and we will explore the effects of these charge transfer states on the solution phase spectroscopy in future work. For the purposes of this article, however, we concern ourselves only with the influence of the different solvent environment on the qualitative dynamics of the underlying trajectories within the covalent manifold.

In Figs. 10 and 11 we thus compare the bondlength histories for our various excited state nonadiabatic dynamical ensembles for A and B state excitation, respectively, in both the argon and xenon matrices. There are several very striking differences in the bondlength trajectories for the different solvents which are evident in these figures. The most dramatic of these differences is clear in the A state excitation results displayed in Fig. 10. In solid xenon the nonadiabatic recombination dynamics results in population in all of the A, A', and X states similar to the situation we saw for B state excitation in argon in Sec. III B. For A state excitation in argon as we saw in Sec. III A, however, we find no evidence of recombination back into the X state and only the A, and A' states are prepared as a result of this excitation and subsequent relaxation in solid argon. We believe that this apparent nonadiabatic dynamical filtering of the recombining
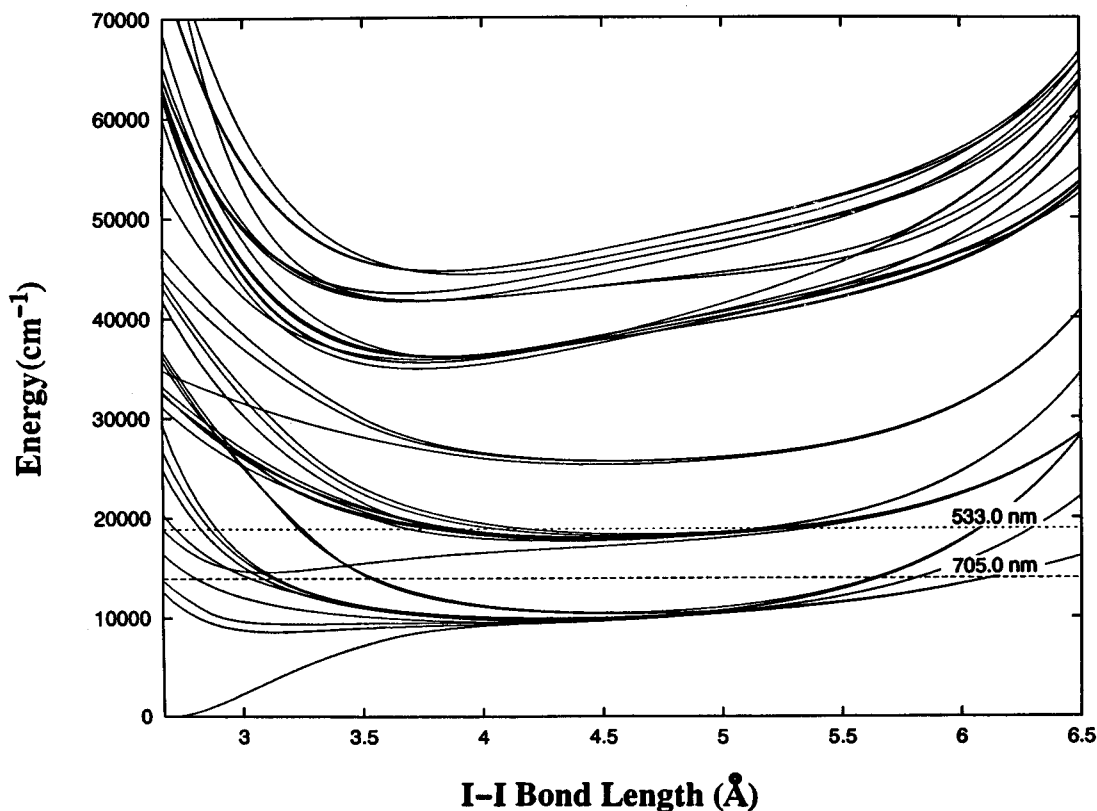

FIG. 9. Same as Fig. 5 only here potential curves for I_2 in a solid xenon matrix with reduced solvent density $\rho^* = 1.16$ are reported. Again A and B state pump excitation energies are indicated.
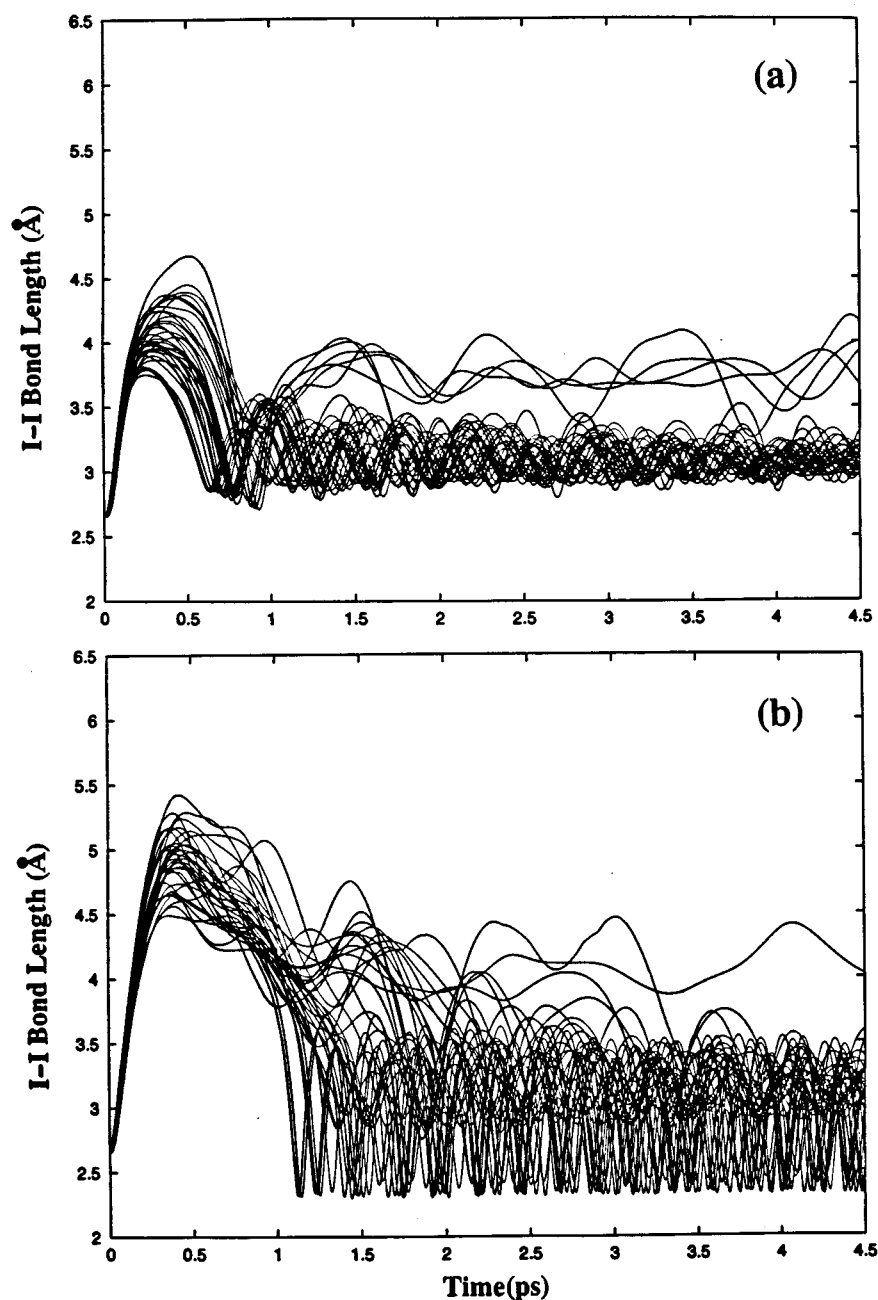
FIG. 10. Comparison of I_2 bond length trajectories following initial A state excitation in (a) solid argon matrices, and (b) solid xenon matrices.

mixed electronic state occurs in argon because of the proximity of the repulsive solvent wall. The gaps between the adiabatic states are large in the tight solvent cavity of the argon matrix and there is less mixing of the X state into the dynamical wave function due to the large energy gap to this state. In xenon where the solvent wall is much further away the coupling will be much smaller so the electronic wave function has the opportunity to become a strong admixture of close lying A, A', and X states. This surprising effect indicates that solvent conditions may provide a subtle way to control mixing of excited electronic states in condensed phase systems.

There are several interesting features to note in Fig. 11

where we compare our B state excitation studies in argon and xenon. First, for this higher energy excitation the recombination dynamics always gives a strongly mixed electronic state at longer times for which the signal is dominated by A, A', and X state absorption apparently independent of solvent, unlike the situation discussed above for the lower energy A state excitation. Next we note that there is a very considerable difference between the argon and xenon solvents in the excited B state vibrational period of trajectories which initially move diabatically and remain in this state out to about 0.8 ps. The excitation conditions are identical but because of the very tight solvent cavity in argon we see nearly three B state vibrational periods with amplitudes near
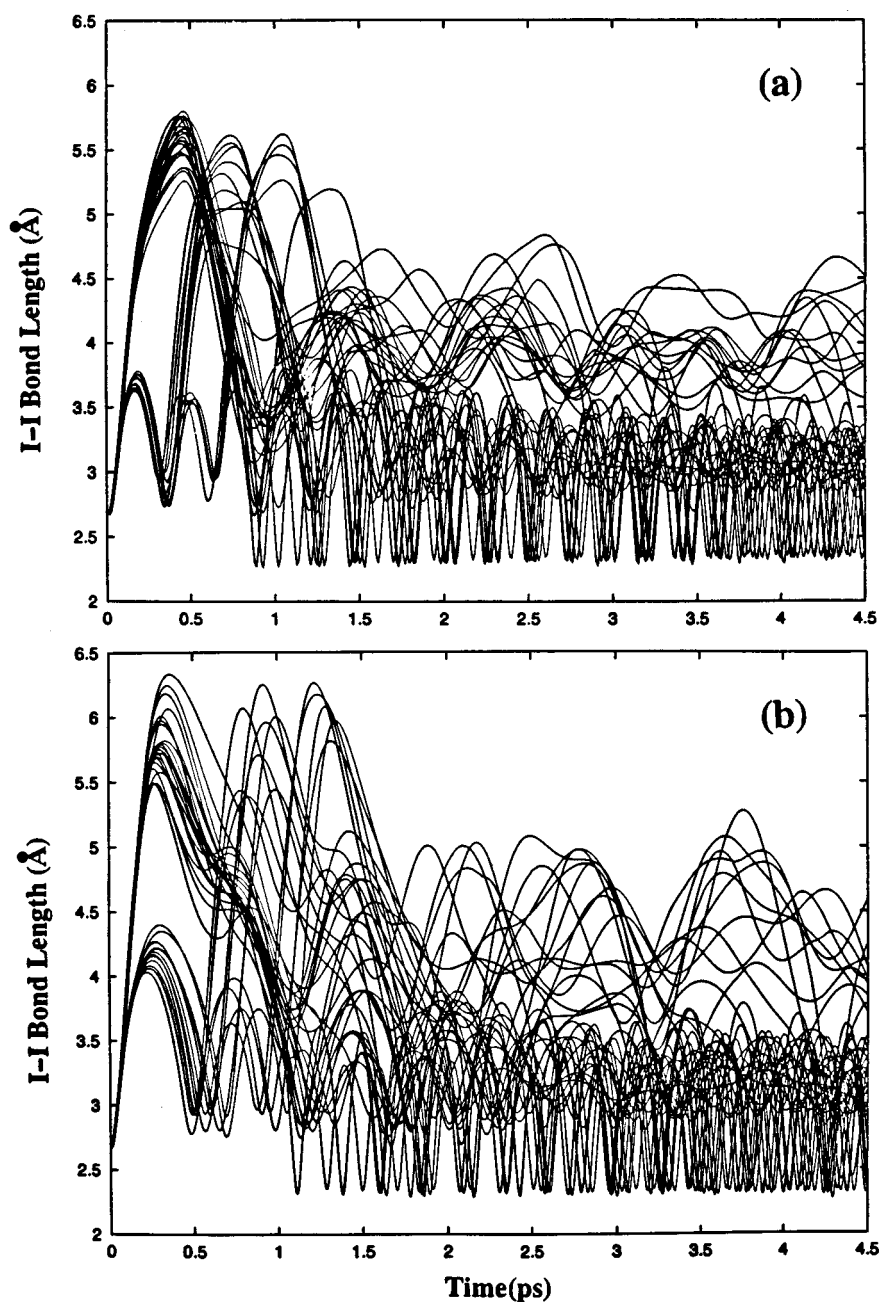
FIG. 11. Comparison of I_2 bond length trajectories following initial B state excitation in (a) solid argon matrices, and (b) solid xenon matrices.

~ 3.5 Å in argon. In xenon, on the other hand, the B state vibrations in the larger solvent cavity extend beyond ~ 4 Å and as a result we see a considerably different excited state vibrational frequency with only two vibrational periods in about 0.8 ps for the xenon matrix.

Experiments on A state excitation in various rare gas matrices[8,14] have revealed small environmental shifts in frequency and anharmonicity for this state. We suggest that an experiment which directly probes the B state vibrational dynamics might be sensitive to the large environmental changes in potential curvature evident in our short time transient results. We have conducted calculations of our absorption signals (equivalent to the experimental laser-induced

fluorescence probe) at shorter wavelengths extending down to 250 nm in the hope that we could separate out a transient B state signal but we find that intense absorptions from the A, A', and X states generally wash out any B state absorption signals. Alternative probing methods (e.g., measurement of dichroic response) might separate out the transient B state signal yielding information on this interesting solvent effect.

The final feature we note which may also be interesting to explore in alternative probing experiments is the establishment of considerable populations of trajectories in states other than the A, A', or X states. From Fig. 11 we see that following B state excitation in either argon or xenon there are many trajectories which undergo very different dynamics

to the bound oscillatory motion of trajectories which simply recombine into the A, A', or X states. These other trajectories show slow undulating bond extensions between about 3.5 and 5 Å with little evidence of any clear periodic motion. We believe that these trajectories primarily involve recombination into the $^3\Sigma_u^+(0_u^-)$ state. From Figs. 5 and 9 this state [and the other highest energy state in the Franck–Condon region from the (3/2,3/2) manifold, the $^3\Delta_u(3_u)$] crosses the B state at the largest bond lengths, and from the intersection of the B state pump wavelength with this curve we see that the inner turning point at just under 3.5 Å matches well with motion in the broad potential well formed by interaction with the fluctuating solvent cage at large R giving an equilibrium position at around 4 Å in argon and $\sim$4.5 Å in xenon in qualitative agreement with the trajectory traces in Fig. 11. Comparing with the A state excitation trajectory results in Fig. 10 we see that this recombination channel is considerably less important for this lower energy dynamics.

IV. CONCLUSION

In this article we have demonstrated the extraordinary predictive potential of coupling accurate semiempirical excited state molecular electronic stucture methods such as DIM and DIIS, with semiclassical nonadiabatic molecular dynamics techniques so that ultrafast electronically excited state molecular relaxation processes in condensed phase systems can be reliably treated. The quantitative agreement between the calculated and experimental ultrafast pump-probe signals exploring A and B state photoexcitation of I_2 in rare gas matrices gives us faith that: (1) the interpretation of the experimental signals emerging from the detailed analysis of our calculated signals presented here is reliable, and (2) it will be very worthwhile pursuing experiments to test the different predictions of these calculations, one of the more intriguing of which is the apparent sensitivity of the cage induced recombination dynamics to solvent environment and pump excitation energy. Our calculations reveal that the recombination pathways can be significantly influenced by both these experimentally adjustable parameters. These studies thus suggest that the pathway of such a complex condensed phase excited state predissociation/recombination reaction might be controlled in a predictable way.

There are dramatic qualitative differences between the experimental B state pump-probe signals in the solid phase,[45] with their coherent vibrational dynamics persisting out beyond 5 ps, and the liquid state (cyclohexane) results of Scherer and co-workers[24] which indicate a rapidly damped dichroic response showing vibrational coherence lasting only for about 0.5 ps. The picture emerging from both the calculations reported here for the solid phase, and our previous liquid phase (xenon) studies of B state excitation[1] is that the underlying early time electronically nonadiabatic relaxation dynamics in either of these condensed phases is remarkably similar; the I_2 molecule undergoes predissociation from the B state via several different channels (predominently the $^1\Pi_u$, $^3\Pi_{2g}$, or a states) on either the 1st, 2nd, or 3rd B state vibrational extension (i.e., between 0.1 and 0.7 ps). In our

liquid state survey study[1] we see subsequent geminate recombination dynamics only at the highest liquid densities studied where only about 25% of our trajectories recombine and do so into the A' state within about 1–1.5 ps after initial excitation. In contrast, *all* B state trajectories in the solid phase calculations reported here undergo rapid predissociation followed by recombination dynamics and into either the A, A', or X states and it is this complete recombination in the solid phase which is responsible for the long time coherent vibrational dynamics observed in the matrix studies.

[1] V. S. Batista and D. F. Coker, J. Chem. Phys. **105**, 4033 (1996).
[2] I. NoorBatcha, L. M. Raff, and D. L. Thompson, J. Chem. Phys. **81** (1984).
[3] Y. J. Yan, R. M. Whitnell, K. R. Wilson, and A. H. Zewail, Chem. Phys. Lett. **193** (1992).
[4] J. Che, M. Messina, K. R. Wilson, V. A. Apkarian, Z. Li, C. C. Martens, and R. Zadoyan, J. Phys. Chem. **100** (1996).
[5] M. Ben-Num, R. D. Levine, D. M. Jonas, and G. R. Fleming, Chem. Phys. Lett. **245**, 629 (1995).
[6] M. Ben-Num and R. D. Levine, Chem. Phys. **201**, 163 (1995).
[7] M. Ben-Num, R. D. Levine, and G. R. Fleming, J. Chem. Phys. **105**, 3035 (1996).
[8] M. Macler, J.-P. Nicolai, and M. C. Heaven, J. Chem. Phys. **91**, 674 (1989).
[9] M. Macler and M. C. Heaven, Chem. Phys. **151**, 219 (1991).
[10] S. Hei, X. Zheng, M. C. Heaven, and J. Tellinghuisen, J. Chem. Phys. **97**, 6057 (1992).
[11] Q. Liu, J. K. Wang, and A. H. Zewail, Nature **364**, 427 (1993).
[12] J. A. Beswick, R. Monot, J. M. Philippoz, and H. van den Bergh, J. Chem. Phys. **86**, 3965 (1987).
[13] O. Roncero, N. Halberstadt, and J. A. Beswick, in *Reaction Dynamics in Clusters and Condensed Phases*, edited by J. Jortner *et al.* (Kluwer Academic, Dordrecht, 1994), pp. 73–87.
[14] P. B. Beeken, E. A. Hanson, and G. W. Flynn, J. Chem. Phys. **78**, 5892 (1983).
[15] R. Zadoyan, Z. Li, C. C. Martens, and V. A. Apkarian, J. Chem. Phys. **101**, 6648 (1994).
[16] N. Schwentner, M. Chergui, H. Kunz, and J. McCaffrey, in *Reaction Dynamics in Clusters and Condensed Phases*, edited by J. Jortner *et al.* (Kluwer Academic, Dordrecht, 1994), pp. 521–537.
[17] A. L. Harris, J. K. Brown, and C. B. Harris, Ann. Rev. Chem. **39**, 341 (1988).
[18] A. L. Harris, M. Berg, and C. B. Harris, J. Chem. Phys **84**, 788 (1986).
[19] M. Berg, A. L. Harris, and C. B. Harris, Phys. Rev. Lett. **54**, 951 (1985).
[20] D. E. Smith and C. B. Harris, J. Chem. Phys **87**, 2709 (1987).
[21] M. E. Paige and C. B. Harris, Chem. Phys **149**, 37 (1990).
[22] M. E. Paige and C. B. Harris, J. Chem. Phys **93**, 1481 (1990).
[23] N. F. Scherer, L. D. Ziegler, and G. R. Fleming, J. Chem. Phys. **96**, 5544 (1992).
[24] N. F. Scherer, D. M. Jonas, and G. R. Fleming, J. Chem. Phys. **99**, 153 (1993).

[25] C. Lienau and A. H. Zewail, J. Chim. Phys. **92**, 566 (1995).

[26] C. Lienau, J. C. Williamson, and A. H. Zewail, Chem. Phys. Lett. **213**, 289 (1993).

[27] C. Lienau and A. H. Zewail, Chem. Phys. Lett. **218**, 224 (1994).

[28] Q. Liu and A. H. Zewail, Chem. Phys. Lett. **218**, 224 (1994).

[29] Q. Liu, C. Wan, and A. H. Zewail, J. Chem. Phys. **105**, 5294 (1996).

[30] P. Y. Cheng, D. Zhong, and A. H. Zewail, J. Chem. Phys. **105**, 6216 (1996).

[31] I. H. Gersonde and H. Gabriel, J. Chem. Phys. **98**, 2094 (1993).

[32] A. I. Krylov, R. B. Gerber, and V. A. Apkarian, Phys. Chem. **189**, 261 (1994).

[33] A. I. Krylov and R. B. Gerber, Chem. Phys. Lett. **231**, 395 (1994).

[34] I. Last and T. F. George, J. Chem. Phys. **87**, 1183 (1987).

[35] I. Last, T. F. George, M. E. Fajardo, and V. A. Apkarian, J. Chem. Phys. **87**, 5917 (1987).

[36] I. Last and T. F. George, J. Chem. Phys. **89**, 3071 (1988).

[37] A. A. Buchachenko and N. F. Stepanov, J. Chem. Phys. **104**, 9913 (1996).

[38] J. C. Tully, J. Chem. Phys. **93**, 1061 (1990).

[39] F. Webster, P. J. Rossky, and R. A. Friesner, Comp. Phys. Comm. **63**, 494 (1991).

[40] S. Hammes-Schiffer and J. C. Tully, J. Chem. Phys. **101**, 4657 (1994).

[41] D. F. Coker and L. Xiao, J. Chem. Phys. **102**, 496 (1995).

[42] Z. Li, R. Zadoyan, V. A. Apkarian, and C. C. Martens, J. Phys. Chem. **99**, 7453 (1995).

[43] W. G. Lawrence and V. A. Apkarian, J. Chem. Phys. **101**, 1820 (1994).

[44] R. Zadoyan, Z. Li, P. Ashjian, C. C. Martens, and V. A. Apkarian, Chem. Phys. Lett. **218**, 504 (1994).

[45] R. Zadoyan, M. Sterling, and V. A. Apkarian, J. Chem. Soc. Faraday Trans. **92**, 1821 (1996).

[46] J. K. Brown, C. B. Harris, and J. C. Tully, J. Chem. Phys. **89**, 6687 (1988).

[47] D. P. Ali and W. H. Miller, J. Chem. Phys. **78**, 6640 (1983).

[48] D. P. Ali and W. H. Miller, Chem. Phys. Lett. **105**, 501 (1984).

[49] R. Boling, J. Langen, and U. Schurath, Chem. Phys. **130**, 419 (1989).

[50] F. O. Ellison, J. Am. Chem. Soc. **85**, 3540 (1963).

[51] F. O. Ellison and J. C. Patel, J. Am. Chem. Soc. **85**, 3544 (1963).

[52] F. O. Ellison and J. C. Patel, J. Am. Chem. Soc. **86**, 2115 (1963).

[53] J. C. D. Brand and A. R. Hoy, Appl. Spectros. Rev. **23**, 285 (1987).

[54] J. Chevaleyre, J. P. Perrot, J. M. Chastan, S. Valignat, and M. Broyer, Chem. Phys. **67**, 59 (1982).

[55] J. Tellinghuisen, J. Chem. Phys. **78**, 2374 (1983).

[56] D. L. Rousseau and P. F. Williams, Phys. Rev. Lett. **33**, 1368 (1974).

[57] J. Tellinghuisen, M. R. McKeever, and A. Sur, J. Mol. Spectros. **82**, 225 (1980).

[58] J. Tellinghuisen, Can. J. Phys. **62**, 1933 (1984).

[59] J. Tellinghuisen, J. Mol. Spectrosc. **94**, 231 (1982).

[60] K. S. Viswanathan and J. Tellinghuisen, J. Mol. Spectrosc. **101**, 285 (1983).

[61] J. P. Perrot, M. Broyer, J. Chevaleyre, and B. Femelat, J. Mol. Spectros. **98**, 161 (1983).

[62] M. L. Nowlin and M. C. Heaven, Chem. Phys. Lett. **239**, 1 (1995). Parameters calculated from the *RKR* potential energy curve obtained from the authors on request.

[63] J. C. D. Brand, A. R. Hoy, A. K. Kalkar, and A. B. Yamashita, J. Mol. Spectros. **95**, 350 (1982).

[64] G. W. King, I. M Littlewood, and J. R. Robins, Chem. Phys. **56**, 145 (1981).

[65] J. C. D. Brand and A. R. Hoy, J. Mol. Spectros. **97**, 379 (1983).

[66] K. S. Viswanathan, A. Sur, and J. Tellinghuisen, J. Mol. Spectrosc. **86**, 393 (1981).

[67] J.C. Tully, *Semiempirical Methods of Electronic Structure Calculation, Part A: Techniques*, edited by G. A. Segal (Plenum, New York, 1977).

[68] E. S. Rittner, J. Chem. Phys. **19**, 1030 (1951).

[69] P. Brumer and M. Karplus, J. Chem. Phys. **58**, 3903 (1973).

[70] C. H. Becker, P. Casavecchia, and Y. T. Lee, J. Chem. Phys. **70**, 5477 (1979).

[71] Y. Zhao, I Yourshaw, G. Reiser, C. C. Arnold, and D. M. Neumark, J. Chem. Phys. **101**, 6538 (1994). MMSV potential contructed from Eqs. (1),(2),(4)-(6), and parameters presented in Table VII.

[72] E. L. Pollock and B. J. Alder, Phys. Rev. Lett. **41**, 903 (1978).

[73] C. J. F. Bottcher, *Theory of Electric Polarization*, edited by Z. B. Maksic (Elsevier, Amsterdam, 1952).

[74] J. Applequist, J. R. Carl, and K-K. Fung, J. Am. Chem. Soc. **94**, 2953 (1972).

[75] A. S. Goldstein and H. Jonsson, Phil. Mag. B **41**, 903 (1995).

[76] A. L. Guy, A. Sur, K. S. Viswanathan, and J. Tellinghuisen, Chem. Phys. Lett. **73**, 582 (1980).

[77] J. Tellinghuisen, Phys. Rev. Lett. **34**, 1137 (1975).

[78] J. Tellinghuisen, Chem. Phys. Lett. **29**, 359 (1974).